DEFENCE **R&D** DÉFENSE

UWB Impulse Radar Characterization and Processing Techniques

Greg Barrie

Canadä

		Form Approved OMB No. 0704-0188

Report Documentation Page

Public reporting burden for the collection of information is estimated to average 1 hour per response, including the time for reviewing instructions, searching existing data sources, gathering and maintaining the data needed, and completing and reviewing the collection of information. Send comments regarding this burden estimate or any other aspect of this collection of information, including suggestions for reducing this burden, to Washington Headquarters Services, Directorate for Information Operations and Reports, 1215 Jefferson Davis Highway, Suite 1204, Arlington VA 22202-4302. Respondents should be aware that notwithstanding any other provision of law, no person shall be subject to a penalty for failing to comply with a collection of information if it does not display a currently valid OMB control number.

1. REPORT DATE **DEC 2004**	2. REPORT TYPE	3. DATES COVERED **-**
4. TITLE AND SUBTITLE **UWB Impulse Radar Characterization and Processing Techniques (U)**		5a. CONTRACT NUMBER
		5b. GRANT NUMBER
		5c. PROGRAM ELEMENT NUMBER
6. AUTHOR(S)		5d. PROJECT NUMBER
		5e. TASK NUMBER
		5f. WORK UNIT NUMBER
7. PERFORMING ORGANIZATION NAME(S) AND ADDRESS(ES) **Defence R&D Canada -Ottawa,National Defence Headquarters,Ottawa,CA,K1A OK2**		8. PERFORMING ORGANIZATION REPORT NUMBER
9. SPONSORING/MONITORING AGENCY NAME(S) AND ADDRESS(ES)		10. SPONSOR/MONITOR'S ACRONYM(S)
		11. SPONSOR/MONITOR'S REPORT NUMBER(S)
12. DISTRIBUTION/AVAILABILITY STATEMENT **Approved for public release; distribution unlimited**		
13. SUPPLEMENTARY NOTES **The original document contains color images.**		

14. ABSTRACT

Ultra-Wideband (UWB) impulse radar is inherently a noise-limited technology. While sub-nanosecond pulses achieve good range resolution, the resultant extreme bandwidth exacts a toll on system performance in terms of noise power entering the receiver. Data must be processed efficiently to yield an acceptable signal to noise ratio (SNR), and to enhance structural details of the return pulse. This is achieved by a combination of ensemble averaging to reduce thermal fluctuations and the newly developed Background Noise Conditioning (BNC) method, a statistical signal processing technique used to remove isolated spectral interferers. BNC, developed at DRDC Ottawa, periodically examines spectral noise properties to automatically configure an appropriate notch filter. For the radar data obtained in this investigation, averaging over a relatively small number of pulses is insufficient to raise the desired returns appreciably above the noise floor. Typical SNR values for one received pulse are around 18 to 19 dB. Beyond ten pulses, SNR improves approximately linearly. Integration of about 80 pulses results in a SNR maximum of about 35 dB with an associated improvement of ~15 dB over the untreated data (that is, for situations where BNC is not applied). For pulses > 80, the averaging takes place over a long enough time period that returns become blurred due to target motion. This effectively defines the upper limit of pulse returns that can be averaged without additional processing to focus the returns. Part of this report is devoted to modeling and characterizing the impulse shape and its associated spectrum. As well, the minimum detectable target velocity is extracted from data and compared with theory, showing good agreement. Wall effects have been investigated-there was an experimental determination of approximately 8dB attenuation losses due to a cindercrete wall. The same wall, once soaked with water, caused only an additional 2dB loss (both of these are one-way measurements). A model for wall-induced clutter is developed, providing expressions for the pulse return shape and duration. The imaging of objects buried in snow, using both 1D ranging and 2D SAR techniques establishes that objects can be located although the current resolution is such that it would make identification challenging. A major concern is the processing technique itself, which is a form of area Moving Target Indicator (MTI), where returns from stationary targets are partially removed in the processing stage. These results will be used to develop algorithms for extracting stationary targets without apriori knowledge of the background.

15. SUBJECT TERMS

16. SECURITY CLASSIFICATION OF:			17. LIMITATION OF ABSTRACT	18. NUMBER OF PAGES	19a. NAME OF RESPONSIBLE PERSON
a. REPORT	b. ABSTRACT	c. THIS PAGE		**82**	
unclassified	**unclassified**	**unclassified**			

UWB Impulse Radar Characterization and Processing Techniques

Greg Barrie
Defence R&D Canada – Ottawa

Defence R&D Canada - Ottawa

Abstract

Ultra-Wideband (UWB) impulse radar is inherently a noise-limited technology. While sub-nanosecond pulses achieve good range resolution, the resultant extreme bandwidth exacts a toll on system performance in terms of noise power entering the receiver. Data must be processed efficiently to yield an acceptable signal to noise ratio (SNR), and to enhance structural details of the return pulse. This is achieved by a combination of ensemble averaging to reduce thermal fluctuations and the newly developed *Background Noise Conditioning* (BNC) method, a statistical signal processing technique used to remove isolated spectral interferers. BNC, developed at DRDC Ottawa, periodically examines spectral noise properties to automatically configure an appropriate notch filter.

For the radar data obtained in this investigation, averaging over a relatively small number of pulses is insufficient to raise the desired returns appreciably above the noise floor. Typical SNR values for one received pulse are around *18 to 19 dB*. Beyond ten pulses, SNR improves approximately linearly. Integration of about 80 pulses results in a SNR maximum of about *35 dB*, with an associated improvement of *~15 dB* over the untreated data (that is, for situations where BNC is not applied). For pulses *> 80*, the averaging takes place over a long enough time period that returns become blurred due to target motion. This effectively defines the upper limit of pulse returns that can be averaged without additional processing to focus the returns. Part of this report is devoted to modeling and characterizing the impulse shape and its associated spectrum. As well, the minimum detectable target velocity is extracted from data and compared with theory, showing good agreement.

Wall effects have been investigated—there was an experimental determination of approximately 8dB attenuation losses due to a cindercrete wall. The same wall, once soaked with water, caused only an additional 2dB loss (both of these are one-way measurements). A model for wall-induced clutter is developed, providing expressions for the pulse return shape and duration.

The imaging of objects buried in snow, using both 1D ranging and 2D SAR techniques establishes that objects can be located, although the current resolution is such that it would make identification challenging. A major concern is the processing technique itself, which is a form of area Moving Target Indicator (MTI), where returns from stationary targets are partially removed in the processing stage. These results will be used to develop algorithms for extracting stationary targets without apriori knowledge of the background.

Résumé

De par sa nature, le radar à impulsions à bande ultra-large (UWB) correspond à une technologie limitée par le bruit. Bien que les impulsions de durée inférieure à une nanoseconde donnent une bonne résolution en distance, la largeur de bande extrême qui en résulte nuit aux performances du système en termes de puissance de bruit entrant dans le récepteur. Les données doivent être traitées efficacement pour produire un rapport signal/bruit (S/B) acceptable et pour rehausser les détails structuraux de l'écho. À cette fin, on utilise une combinaison de l'établissement de la moyenne d'ensemble afin de réduire les fluctuations thermiques et de la méthode récemment élaborée de *conditionnement de bruit de fond* (BNC), technique de traitement statistique des signaux utilisée pour éliminer les signaux brouilleurs spectraux isolés. Le BNC, élaboré par RDDC Ottawa, examine périodiquement les propriétés du bruit spectral en vue de configurer automatiquement un filtre coupe-bande approprié.

Pour les données radar obtenues au cours de cette étude, l'établissement d'une moyenne pour un nombre d'impulsions relativement petit ne suffit pas pour porter les échos voulus notablement au-dessus du bruit de fond. Les valeurs types du rapport S/B d'une seule impulsion reçue sont de l'ordre de *18 à 19 dB*. Au-delà de dix impulsions, le rapport S/B s'améliore de façon à peu près linéaire. L'intégration d'environ 80 impulsions donne lieu à un rapport S/B maximal d'environ *35 dB*, avec une amélioration associée de *~15 dB* des données non traitées (c.-à-d. pour les cas où le BNC n'est pas appliqué). Pour plus de *80* impulsions, l'établissement de la moyenne a lieu pendant une période assez longue pour que les échos soient brouillés à cause du déplacement de la cible. Cela définit effectivement la limite supérieure des échos dont un peut établir la moyenne sans traitement supplémentaire pour cibler les échos. Une partie de ce rapport est consacrée à la modélisation et à la caractérisation de la forme d'impulsion et du spectre connexe. De plus, la vitesse minimale détectable de la cible est extraite des données et comparée avec la valeur calculée : il y a une bonne concordance.

On a étudié les effets de paroi — une expérience a permis de déterminer un affaiblissement d'environ 8 dB dû à une paroi en béton de mâchefer. La même paroi, trempée d'eau, causait un affaiblissement supplémentaire de seulement 2 dB (dans les eux cas, il s'agissait de mesures unidirectionnelles). Un modèle est élaboré pour le clutter dû à la présence d'une paroi, permettant d'exprimer la forme et la durée des échos.

L'imagerie d'objets enfouis dans la neige, au moyen de techniques de télémétrie 1D et de techniques RSO 2D, a permis d'établir que ces objets peuvent être localisés, bien que la résolution actuelle soit telle que l'identification poserait un défi. Une des préoccupations principales est la technique de traitement elle-même, qui fait appel à une forme d'indication de cibles mobiles (MTI) de zone, et dans laquelle les cibles fixes sont partiellement éliminées au stade de traitement. Ces résultats seront utilisés pour élaborer des algorithmes pour extraire les cibles fixes sans connaissances a priori du bruit de fond.

Executive summary

Defence R&D Canada (DRDC) has an active research program in many aspects of Ultra-Wideband (UWB) radar systems, including simulation, data analysis and hardware prototyping. UWB impulse (or short-pulse) radars are capable of producing high-resolution images by combining the performance benefits of sub-nanosecond impulse technology and synthetic arrays. One particular application of this is in the area of through-wall sensing, where relatively low center frequencies enable good radio frequency (RF) penetration of typical building materials. Another application involves the use of UWB radar systems for search and rescue of avalanche victims. This is a Canadian multi-department venture including Parks Canada, the National Search and Rescue Secretariat, and the Department of National Defence.

This report outlines the current target discrimination capabilities of UWB impulse radar systems to operate through simple building materials and snow. While sub-nanosecond pulses achieve good range resolution, the resultant extreme bandwidth exacts a toll on system performance in terms of noise power entering the receiver. Impulse radar lacks the filtering and down-conversion of narrowband systems, and individual returns are severely impaired by thermal noise, clutter and external interference. Consequently, UWB impulse radar is inherently a noise-limited technology.

To compensate, data must be processed to yield an acceptable SNR, and to enhance structural details of the return pulse. This is achieved by a combination of ensemble averaging to reduce thermal fluctuations, and application of the newly developed *Background Noise Conditioning* (BNC) method, a statistical signal processing technique used to remove isolated spectral interferers. BNC, developed at DRDC Ottawa, periodically examines spectral noise properties to automatically configure an appropriate notch filter. Another attribute considered in this report is the measurement of target velocity, traditionally obtained in narrowband systems via the Doppler frequency shift arising from target motion. Impulse radar systems are baseband, and have no carrier frequency to exploit. However, this information can be obtained directly in the time-domain by measuring changes in pulse arrival times.

This report demonstrates improved target discrimination capability, achieving enhanced signal to noise ratios (SNR), and verification of target velocity thresholds using experimentally obtained data. These results will be used to develop algorithms for extracting both moving and stationary targets without apriori knowledge of the background. One approach could be to establish a data bank of target signatures and use these to process data returns via correlation techniques.

Barrie, G., 2004. UWB Impulse Radar Characterization and Processing Techniques. DRDC Ottawa TR 2004-251. Defence R&D Canada - Ottawa.

Sommaire

R & D pour la défense Canada (RDDC) a un programme de recherche active sur bien des aspects des systèmes radar à bande ultra-large (UWB), y compris la simulation, l'analyse des données et le prototypage matériel. Les radars à impulsions (ou à impulsions courtes) UWB sont capables de produire des images à haute résolution en combinant les avantages de performance de la technologie des impulsions de durée inférieure à une nanoseconde et le radar à synthèse d'ouverture. Une application particulière de cette technique est dans le domaine de la détection à travers une paroi, où des fréquences centrales relativement basses permettent une bonne pénétration RF de matériaux de construction types. Une autre application concerne l'utilisation de systèmes radar UWB pour la recherche et le sauvetage de victimes d'avalanche. Il s'agit d'une entreprise canadienne pluriministérielle comprenant Parcs Canada, le Secrétariat national de recherche et sauvetage et le ministère de la Défense nationale.

Le présent rapport décrit les capacités actuelles de discrimination de cibles des systèmes radar à impulsions UWB à travers de simples matériaux de construction et la neige. Bien que les impulsions de durée inférieure à une nanoseconde donnent une bonne résolution en distance, la largeur de bande extrême qui en résulte nuit aux performances du système en termes de puissance de bruit entrant dans le récepteur. Le radar à impulsions est dépourvu du filtrage et de la conversion vers le bas des systèmes à bande étroite, et les échos individuels sont fortement altérés par le bruit thermique, le clutter et le brouillage externe. Par conséquent, de par sa nature, le radar à impulsions UWB correspond à une technologie limitée par le bruit.

Pour y remédier, les données doivent être traitées pour produire un rapport S/B acceptable et pour rehausser les détails structuraux de l'écho. À cette fin, on utilise une combinaison de l'établissement de la moyenne d'ensemble afin de réduire les fluctuations thermiques et de l'application de la méthode récemment élaborée de *conditionnement de bruit de fond* (BNC), technique de traitement statistique des signaux utilisée pour éliminer les signaux brouilleurs spectraux isolés. Le BNC, élaboré par RDDC Ottawa, examine périodiquement les propriétés du bruit spectral en vue de configurer automatiquement un filtre coupe-bande approprié. Un autre aspect considéré dans le présent rapport est la mesure de la vitesse de la cible, obtenue jusque-là au moyen de systèmes à bande étroite grâce au décalage Doppler produit par le déplacement de la cible. Les systèmes radar à impulsions fonctionnent en bande de base et ne peuvent pas mettre en valeur une fréquence porteuse. Toutefois, l'information de vitesse peut être obtenue directement dans le domaine temps par mesure de la variation du temps d'arrivée des échos.

Le présent rapport démontre la capacité améliorée de discrimination de cibles, l'obtention de meilleurs rapports signal/bruit (S/B) et la vérification de seuils de vitesse des cibles au moyen de données expérimentales. Ces résultats seront utilisés pour élaborer des algorithmes pour extraire les cibles fixes sans connaissances a priori du bruit de fond. Une des approches possibles consisterait à établir une banque de données de signatures de cibles et à utiliser ces données pour traiter les échos au moyen de techniques de mise en corrélation.

Table of contents

List of figures

List of tables

Acknowledgements

This page intentionally left blank.

1.   Introduction

Defence R&D Canada (DRDC) has an active research program in many aspects of Ultra-Wideband (UWB) radar systems, including simulation, data analysis and hardware prototyping. One particular application is in the area of through-wall sensing, where relatively low center frequencies enable good radio frequency (RF) penetration of typical building materials. A second application involves the use of UWB radar systems for search and rescue of avalanche victims. This is a Canadian multi-department venture including Parks Canada, the National Search and Rescue Secretariat, and the Department of National Defence.

UWB radars are capable of producing high-resolution images by combining the benefits of sub-nanosecond impulse technology and synthetic arrays. A challenging but nonetheless necessary requirement for military, and civilian application of UWB radar is the ability to detect and characterize possible targets through relatively dense, inhomogeneous materials.

Previous work in UWB impulse radar has focused on modeling and simulation [1-3] and on broad, theoretical system-level aspects [4-6], rather than the processing of experimentally obtained data. This document attempts to address the imbalance by undertaking an investigation of how best to process and extract useful information from experimental data. The original impetus for this investigation was to examine the feasibility of standoff application for UWB radar surveillance. Some of the questions addressed are:

- How easily can a target be observed, and at what range?

- How many pulses need to be integrated to obtain a good signal, and how can this be quantified?

- Using a sphere as a target means the RCS is approximately constant, but how well does the Friis transmission formula apply for impulse signals?

- Given the variable nature of the signal (i.e., non-sinusoidal), how can we best determine performance metrics such as SNR?

- What is the typical noise background and what are the characteristics of the RF channel?

- What is the spectral response?

This report outlines progress that has been achieved in target discrimination capability, achieving enhanced signal to noise ratios (SNR), and verification of target velocity thresholds. After a brief discussion of the experimental configuration, the following subjects are examined:

Filtering and noise reduction — UWB impulse radar is inherently a noise-limited technology. While sub-nanosecond pulses achieve good range resolution, the resultant extreme bandwidth exacts a toll on system performance in terms of noise power entering the

receiver. This section examines ways to efficiently process the raw data to achieve acceptable Signal to Noise levels.

Signal characterization — Impulse waveforms are baseband–there is no dominant frequency component as is the case with narrowband. The question arises then on how to best characterize the signal. Since the very act of transmission distorts the signal we need a better understanding of its properties in both time and frequency domains.

System performance — The experimental apparatus described in this report is not as much a radar system as a collection of instruments for transmission and sampling of data. Nevertheless, we can still piece together some of the operating parameters to estimate the performance in terms of signal to noise ratio and propagation phenomena.

Target velocity processing — Impulse radar transmissions are carrier-free and therefore unable to exploit Doppler processing. However, target motion is still observable by examining changes in target range from pulse to pulse. The basis for processing now becomes the change in arrival time of the pulse. In effect, we employ a form of *Area Moving Target Indicator (Area MTI)*, comparing the complex envelopes of successive scans to identify target motion. This section develops the governing equations for minimum detectable velocity, and demonstrates how this information can be extracted from experimental data.

Wall considerations — As concrete was selected to be the building material of interest for this project, we need to determine the effects of moisture content on signal propagation and attenuation. To our knowledge, little has been mentioned in the literature regarding moisture content and to what extent it will increase attenuation. Accordingly, a concrete block (cindercrete) wall was constructed to obtain transmission loss data for both dry and wet blocks.
Additionally, for through-wall imaging the building material acts as a reflector, with its own characteristic radar cross section (RCS). This section describes an adaptation of altimeter radar applied to wall-induced clutter, and derives expressions for the shape and duration of wall reflections.

Application to avalanche victim detection — In any two- or three-dimensional radar imaging system, the basic element of target information is a time-delayed impulse response. This section first examines one-dimensional range data to measure radar returns from various objects buried in a mound of snow, and then supplies some recent results from 2D SAR processing.

2. Data collection

A series of experiments were carried out using an improvised UWB radar system (see Figure 1) to track the motion of a metallic sphere as it rotates about a fixed point. From trial to trial, the nominal range remained fixed while the motion of the sphere traced out a circular path one meter in diameter. Sets of data were recorded for the following ranges: 7, 14, 21, 28, 35, 42, and 49m. Essential to any imaging application is the collection of raw data for further processing. This configuration provides a means of generating and transmitting short-time pulses, collecting the return from a reflecting target, and associating with that echo a return-time delay. The resulting data was collected and written onto a disc for post-processing.
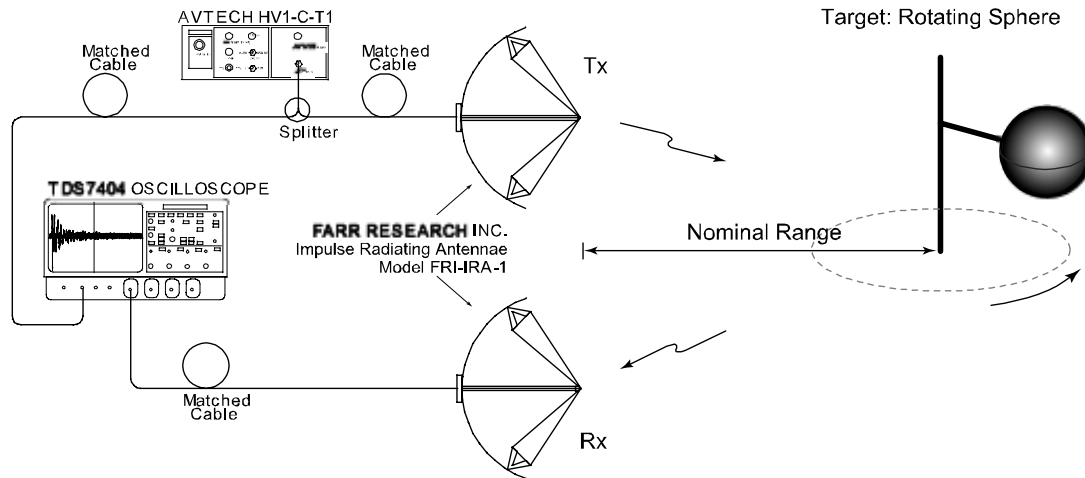
Figure 1. Configuration for data collection.

The data was collected in frames of 2000 samples each[1], with sampling increments of 50ps (sampling frequency of 20GHz), to provide a frame duration of 100ns. The pulse repetition frequency was set at 1kHz[2], resulting in a pulse-to-pulse interval of 1ms. The elapsed time at any given frame is therefore k x 1ms, where k = frame number. For longer ranges, the oscilloscope trigger time was delayed to keep the returns in the desired range gate. A typical target return is shown in Figure 2. Features to note are the prominent return at 14m, representing the sphere, and another, less coherent, but strong, signal at the origin. This is leakage from the transmit antenna, and as it turns out, is an unavoidable artifact since it is this transmitted pulse that is used to set the trigger on the oscilloscope. In between these two returns is a region dominated by thermal noise, external interference and clutter, referred to on the whole as *background noise*. Part of this document examines ways to minimize the influence of this.

---

[1] Tektronix sampling oscilloscope model TDS-7404.
[2] AVTECH pulse generator model AVH-HV1-C-T1
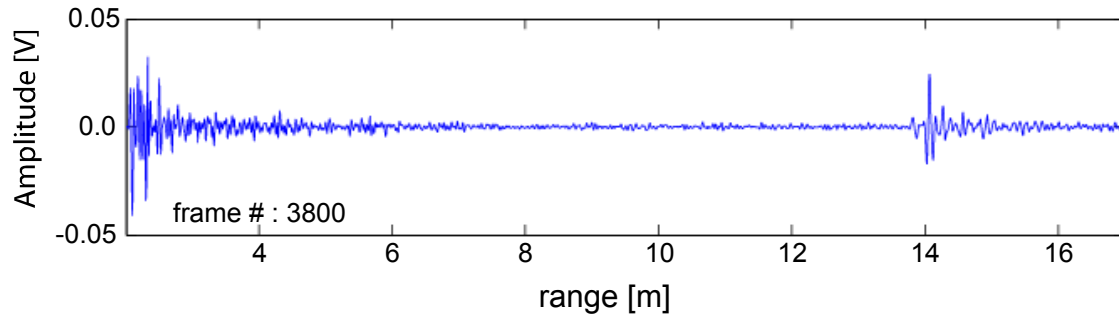
Figure 2. *Target return at 14m.*

The configuration depicted in Figure 1 is obviously not an operational SAR system, but it *can* be considered equivalent to a single element, or discrete position, within the synthetic array. With this single-platform, monostatic arrangement, we are effectively reduced to a one-dimensional ranging device, since there is no way to distinguish angles of arrival. However, as will be developed later in the report, the motion of the target can be used to our advantage in developing an *Inverse* SAR (ISAR) processor.

3.   Filtering and noise reduction

UWB impulse radar is inherently a noise-limited technology. While sub-nanosecond pulses achieve good range resolution, the resultant extreme bandwidth exacts a toll on system performance in terms of noise power entering the receiver.

As is typical of impulse radar returns that lack the filtering commonplace in narrowband systems, individual returns are severely impaired by thermal noise, clutter and external interference. A variety of noise sources impact the filtering requirements of UWB impulse radar systems:

- out-of-band interference

- in-band interference

- thermal noise

Data must be processed efficiently to yield an acceptable signal to noise ratio (SNR), and to enhance structural details of the return pulse. This is achieved by a combination of ensemble averaging to reduce thermal fluctuations and the newly-developed *Background Noise Conditioning* (BNC) method, a statistical signal processing technique used to remove isolated spectral interferers [7]. The BNC algorithm periodically examines spectral noise/interference characteristics, and automatically configures an appropriate notch filter.

3.1   Out-of-band interference

Interfering sources that lie outside of the band of interest can be removed by standard filtering techniques [8]. In the early stages of this investigation, data was processed offline. In that situation, a bandpass filter was implemented in software. Specifically, a 15-tap FIR filter with a passband of 1.5 to 3.0 GHz was applied. The frequency and phase response are displayed in Figure 3. A Hamming window was applied and the output normalized so that the magnitude response is 0dB at the center frequency.
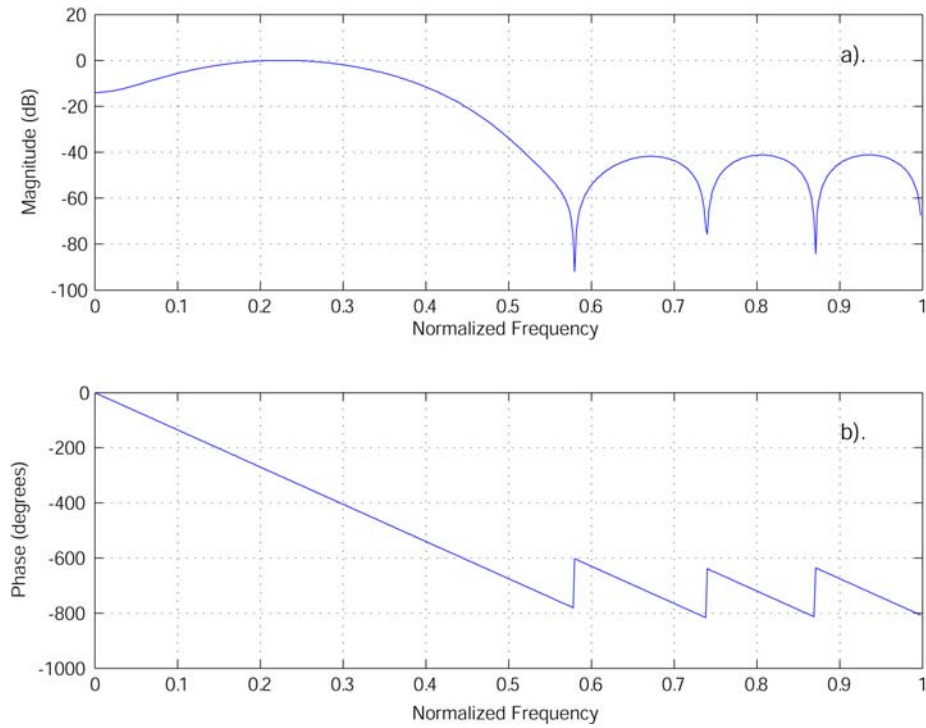
Figure 3. *Response characteristics of numerical filter.*

More recently, hardware was purchased from Mini-Circuits to carry out band pass filtering as data is collected. A practical aspect of these filters (SHP-1000 and SLP-2950) is the SMA-type connector, allowing easy addition or removal from our prototype system. The measured response is shown in Figure 4a. Two sets of such filters were combined to produce a cascaded system as displayed in Figure 4b.
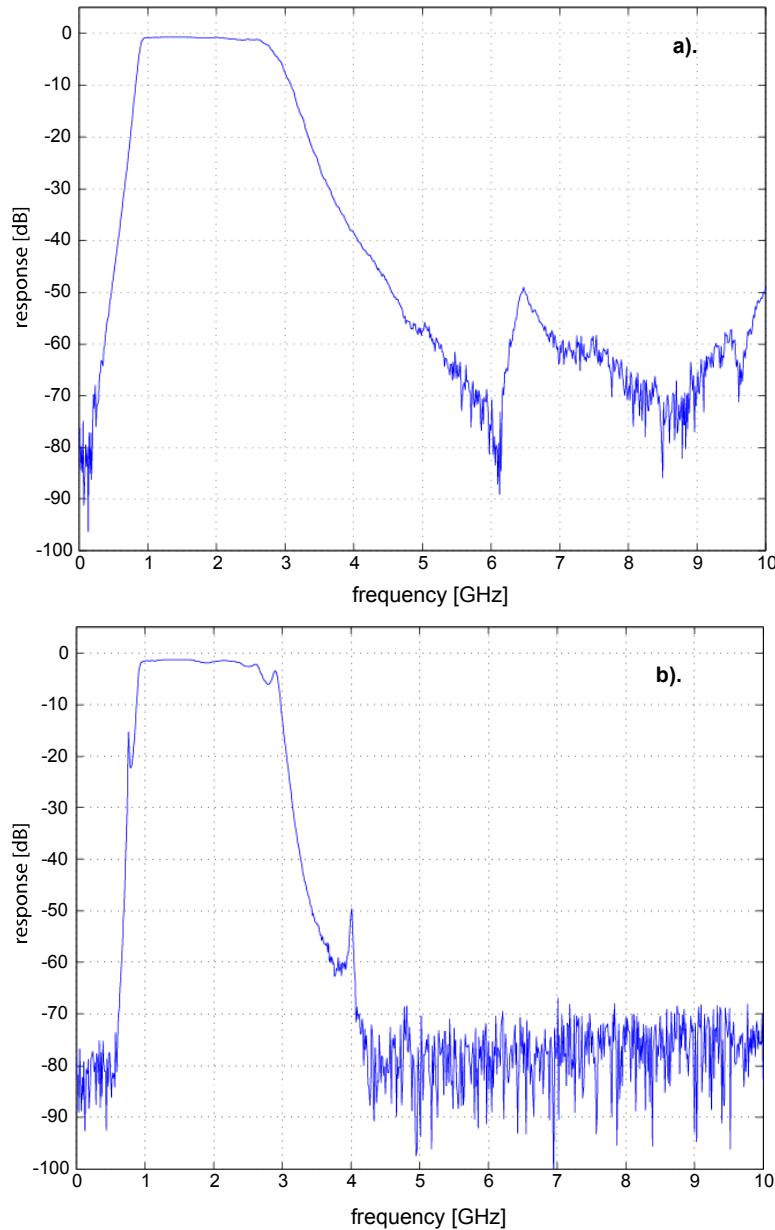
Figure 4. *Mini-Circuits measured filter response.*
a). single highpass/lowpass combination;
b). two cascaded highpass/lowpass filters.

3.2   In-band interference

Removing in-band interference is somewhat more problematic. By its very definition, wideband transmission allows interfering sources to enter the receive chain. Further, the interference exists in two main forms—relatively narrowband "discrete" sources and broadband noise; we require different approaches to remove these impairments.

Consider for example, the frequency spectrum displayed in Figure 5. This data was obtained passively, that is, the radar was not transmitting at the time. This is an indication of typical noise background[3]. Interspersed throughout the spectrum is a range of relatively large spectral components, each of which contributes to the overall received signal, introducing artifacts in the waveform.
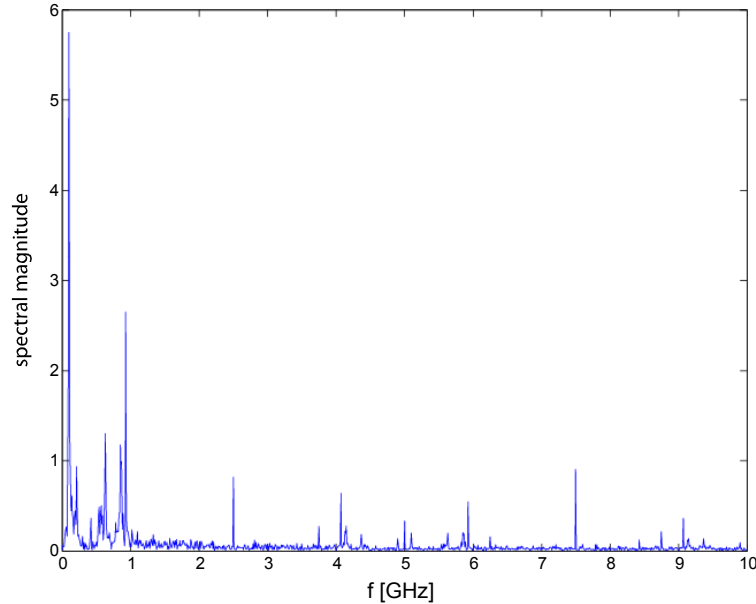
Figure 5. *Background noise, no radar signal present*
(dc component removed, $f_s = 20GHz$).

3.3   Background noise conditioning

To better gauge the effect of noise and interference on the signal, major peaks were first identified and a filter was designed to "notch-out" the undesired components. The result was the removal of low-frequency ripples in the waveform, leading to an improvement in SNR.

The problem with this approach is that it requires human intervention to identify unwanted components. As we have no reason to assume background noise will remain stationary, the notch filter constructed at one moment will not always apply the next. Even with a signal present as in Figure 6, we readily observe a number of peaks, but most are out of the bandwidth of interest, which extends up to approximately 4GHz. Only one distinct peak at approximately 2.5GHz is visible. Components buried within the signal are the major concern in this situation.

---

[3] Additional samples were obtained at different times and different locations. The plot shown here is qualitatively similar to other data sets.
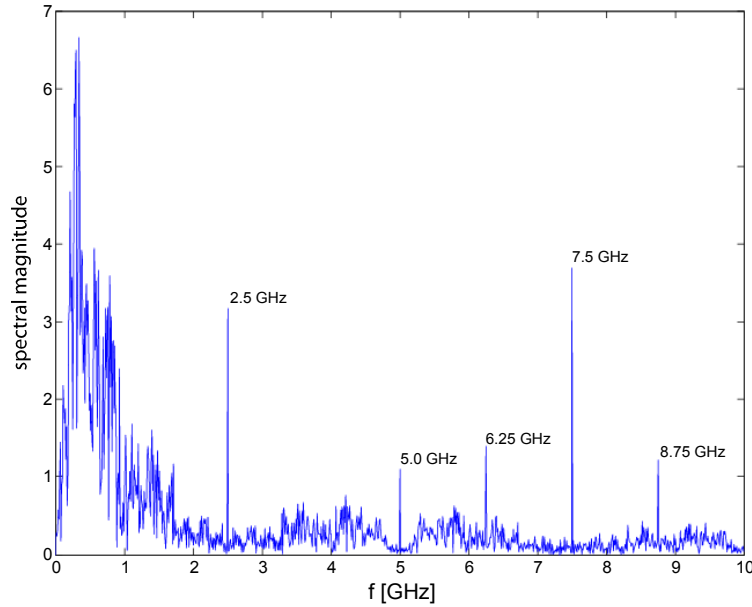
Figure 6. *Raw, unfiltered spectral data (dc component removed).*

To address this, an algorithm was developed to automatically configure an appropriate notch filter. The basic principle of operation is that relatively few spectral components will exceed a given value, and will be observed in the spectrum as spikes (refer again to Figure 5). Since we do not apriori know this cut-off, it is difficult to provide a specific value for which we could consider that component a spike.

A systematic approach to this is to examine the statistical properties of background noise. For example, by using the spectral data to generate a histogram showing the relative frequency vs. spectral magnitude (Figure 7), one can obtain an estimate for the probability distribution *f(x)*, of the noise. Following this, the method mimics standard radar detection techniques where an amplitude threshold value, *ξ*, distinguishes noise from signal power. Empirically, it was found that acceptable performance resulted when the cut-off was set at *P(ξ) = 0.97*, where formally,

$$P(\xi) = \int_{0}^{\xi} f(x)\, dx. \tag{1}$$

This technique is called *Background Noise Conditioning*. The variable *x* represents spectral magnitude. The phrase "acceptable performance" is somewhat subjective, but in general terms the processed signals displayed a noticable improvement in SNR (> 6dB) without significant change to the overall structure of the waveforms.
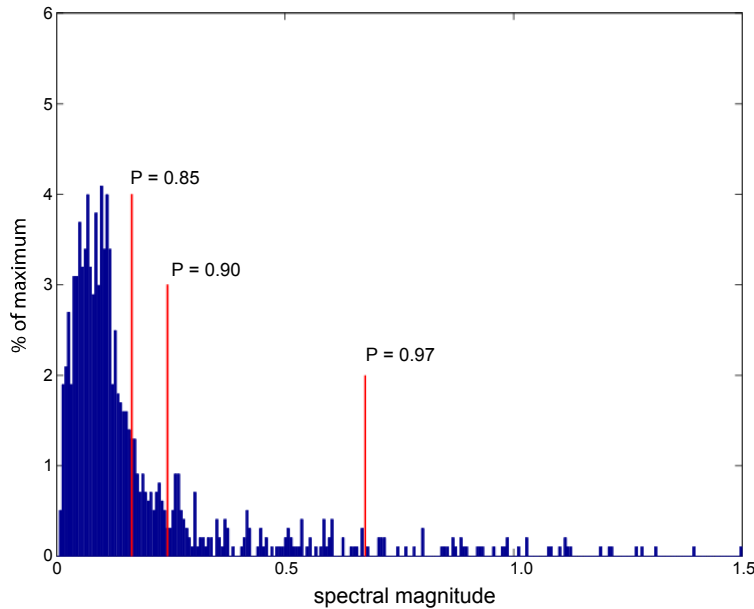
Figure 7. *Typical probability density function f(x) of background noise frequency spectrum.*

It is envisioned that in operational radar, this type of processing could be carried out by periodically suppressing a pulse, with the receiver listening passively. Over time, a database could be established, generating a set of best-fit parameters to model a representative pdf such as, say, a lognormal or a Rayleigh distribution.

3.4   Thermal noise

Due to the spectral content of UWB impulse signals, commonly used narrowband filtering methods are not helpful. The extreme bandwidth, together with a lack of carrier signal means we have no recourse to heterodyning techniques and the ensuing intermediate frequency (IF) filtering. To obtain a useable SNR, the system performs multiple sample integrations to "average out" noise fluctuations.

This technique is applied to UWB processing in the form of *ensemble averaging*. To enhance signal levels, multiple frames are collected for processing. A number of features remain relatively unchanged across frames. This could include:

- Stationary objects in the illumination area

- Effects of system ringing (for example, antennas, cabling, instrumentation effects)

- Coupling of pulses from transmit to receive antenna.

Impairments of this type must be removed from the raw data. In a monostatic configuration, returns are localized, occurring at the same time position (range) from frame-to-frame. Removal is relatively easy with the use of *ensemble averaging*.

Here we consider the collection of a fixed number of data frames, and perform a running average to reduce noise fluctuations. For each block of M frames, the resultant is then subtracted from successive data sets to eliminate stationary signal components. Note that for a bistatic or multistatic configuration, application of this method is not as simple because the relative positions of scatterers will change depending on the particular Tx or Rx antenna element.

As an example of how fluctuations are reduced, we consider a white noise source, as portrayed in Figure 8. The effects of the averaging are summarized in Table 1. In this context, N denotes the number of frames averaged to produce the trace. A running average is obtained with the following lines of Matlab code:

```
for k = 1:N                    % loop over # averages
        X = rand(2000,1):      % random vector
        sum = sum + X;
        av = sum/k;            % compute running average
end
```

This "ideal" white noise source acts as a reference for comparison with collected radar data.
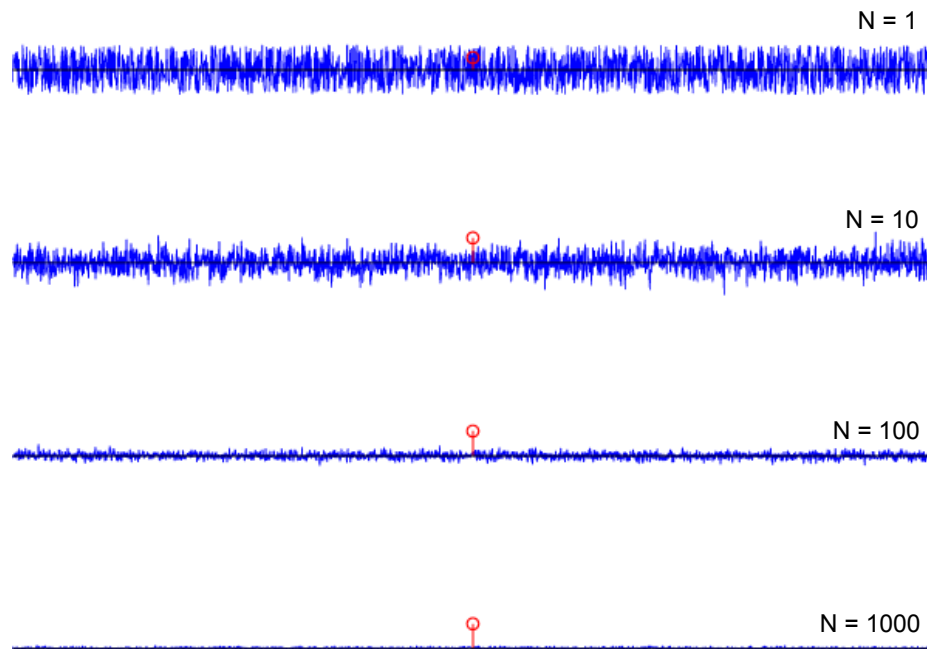
Figure 8. *Example of averaging to improve SNR. The plots show how averaging reduces noise variance to extract a signal of interest (units are arbitrary).*

In this example, we see that an arbitrary signal of constant amplitude is initially undetectable given the noise background. As the number of frames averaged, N, increases, the signal to noise ratio (SNR) continually improves. By reducing noise variance, the averaging provides an effective gain of approximately $G \approx 10 \log_{10} N$, with respect to a single pulse.

Table 1. *Representative processing gains achieved from noise averaging.*

# averages, N	noise variance, σ^2 [dB]	SNR [dB]
1	-4.8	-4.3
10	-14.8	5.7
20	-18.1	9.1
50	-21.8	12.7
100	-24.8	15.8
1000	-34.6	25.5

3.5   SNR improvement

The improvement in signal quality can be quantified by examining the signal-to-noise ratio (SNR) and noise variance. The improvement factor for an idealized noise source has already been examined. In this section, we consider two cases, one in which the radar data is processed by bandpass and notch filtering and is averaged over a number of frames to reduce fluctuations. The second case is where the data is once again averaged, but is not filtered.

The variance σ^2, follows a *1/N* trend as is expected for noise power reduction, but starts to flatten out at higher values of *N* (Figure 9).
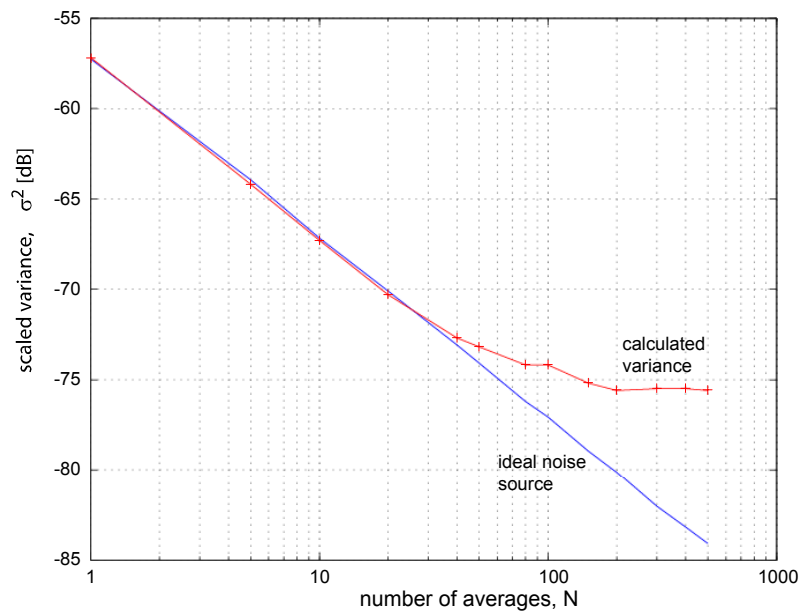
Figure 9. *Idealized and actual variance (signal performance).*

This deviation can be explained by understanding that the actual returned signal is not composed entirely of thermal fluctuations–there are components from the target that have relatively large amplitude in comparison to the background. As the number of frames averaged increases, the influence of the target returns increases with respect to the "pure"

noise, resulting in a greater variance. This is the trend displayed in Figure 9. The two plots have been scaled to align for *N=1*, a single pulse.

An idealized SNR can be calculated as $SNR = -10\log_{10}(\sigma^2)$, where the reference signal is set to unity. However, actual SNR performance (Figure 10), shows a drastic departure from the ideal noise source.
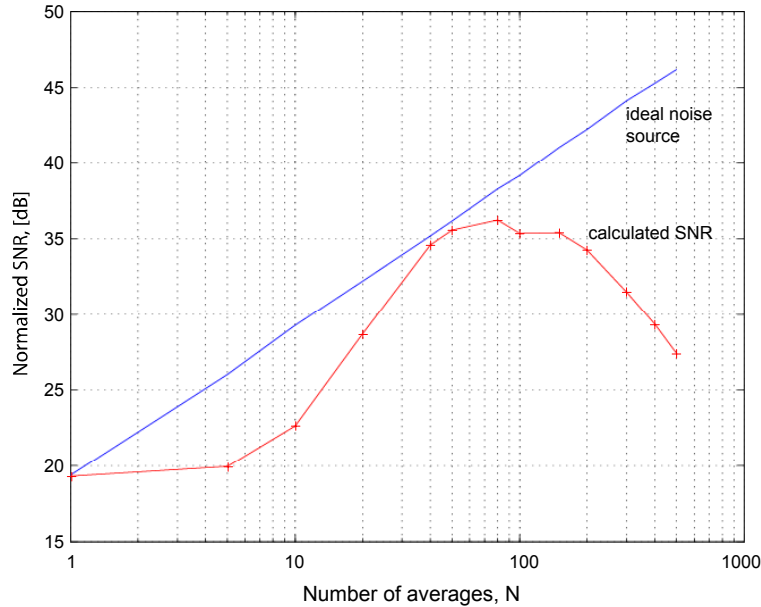
Figure 10. *Idealized and actual SNR performance.*

For the radar data displayed in this figure, averaging over a relatively small number of pulses is insufficient to raise the desired returns appreciably above the noise floor. Typical SNR values at *N* = 1 are around 18 to 19 *dB*, and the trend does not initially follow that of the ideal noise source. A possible explanation for this is that not enough signal energy is collected for lower values of *N*. The idealized curve is white noise, something only approached for large *N* in the case of collected data; the overall result is a smaller target signal response in the presence of relatively large noise contributions.

Beyond this, SNR improves, and does so at a rate comparable to white noise. In this particular instance, SNR peaks at approximately 35 *dB*, an overall improvement of ~15 *dB*. For greater values (for example, *N* > 80), the averaging takes place over a long enough time period that energy is spread due to target motion. This effectively defines the upper limit of *N* that can be achieved without additional processing to focus the returns. In Figure 10 this is the point where the calculated SNR flattens out, and then begins to decrease with *N*. The effects on the pulse itself are observed in Figure 11.

N = 10   unfiltered

filtered

N = 100

N = 500
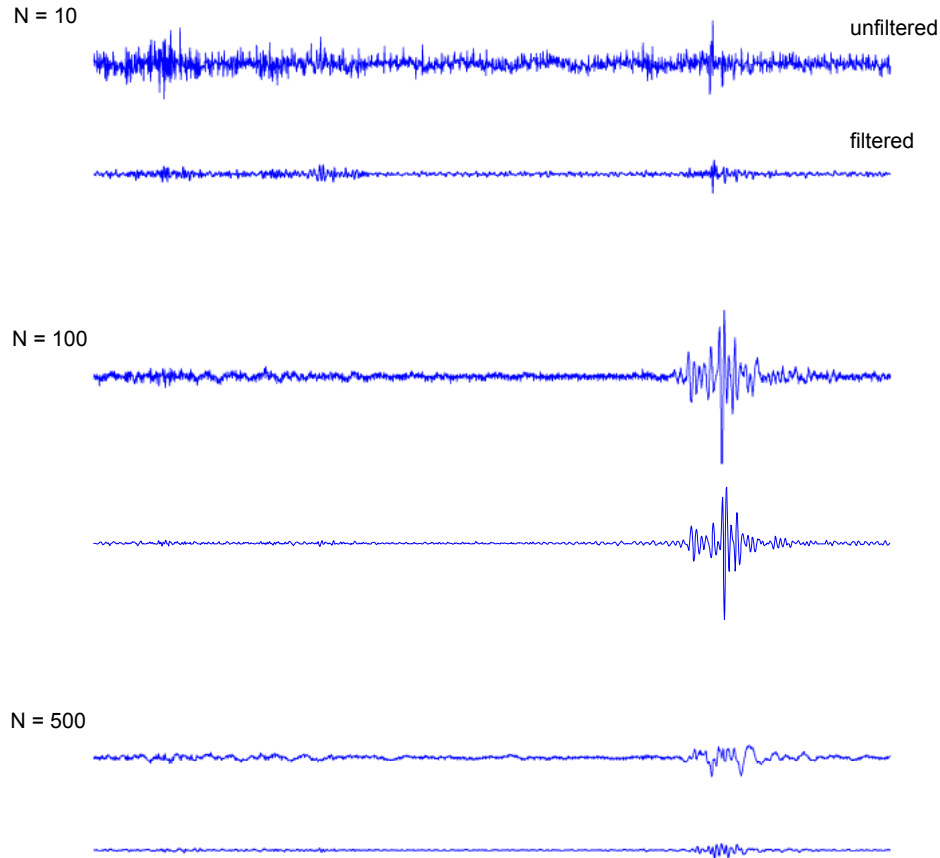
Figure 11. Received signal traces (N=10, 100, 500; range = 21m).

This diagram contains information on a variety of trends. There are three pairs of plots, with pulse returns for $N = 10$, 100 and 500. In turn, each pair shows the outcome of unfiltered processing (top) and filtered processing (bottom). That is, *filtering* includes the application of a bandpass filter for 1 to 3GHz, and background noise conditioning as described previously. Examining the trend, it is obvious that filtering eliminates much of the underlying interference. For example, a low-frequency oscillation is plainly visible in the topmost trace, but the combination of bandpass and notch filtering removes this. To remove the higher frequency fluctuations, we employ the ensemble averaging technique, with the outcome displayed in the bottom traces. As N increases, more and more of the fluctuations are removed, but the target return begins to disperse again, due to target motion. The trace for $N = 500$ corresponds to the rightmost point of Figure 10, where the calculated SNR is far past its peak value.

A more quantitative description of this is contained in Figure 12, comparing SNR and variance as functions of N for both filtered and unfiltered data. From the processing described here, we are able to improve the signal to noise ratio from a minimum of $\sim$ 3dB at N = 1 to a maximum of 7.4dB at $N = 40$.
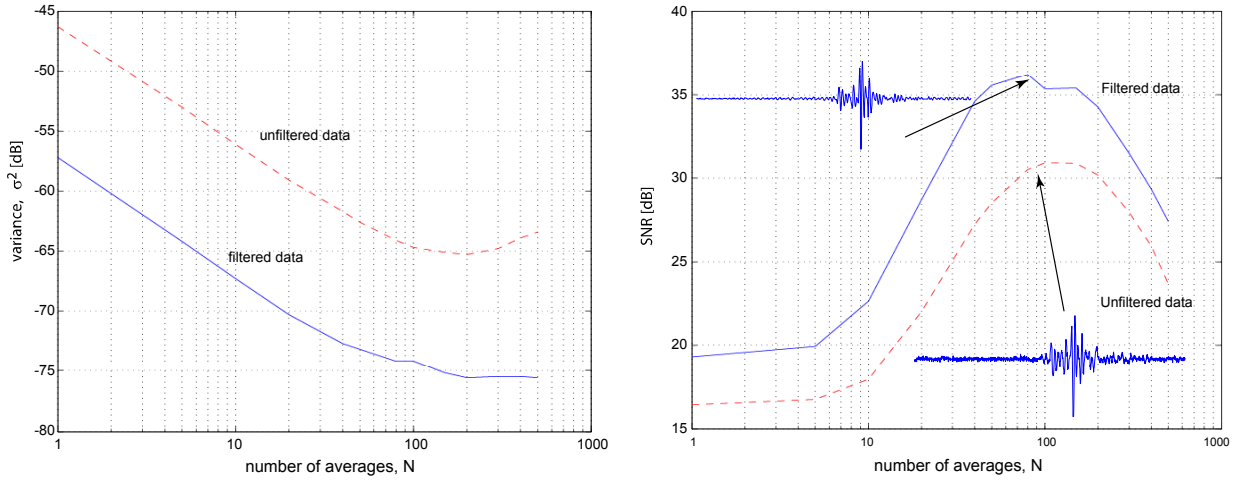
Figure 12. *Variance and SNR vs. N for both filtered and unfiltered data.*

Figure 13 contains an example of improved resolution, showing the fine structure of a pulse return. As much of the processing involves analytic signals, the amplitude (complex envelope) is superimposed on the trace.
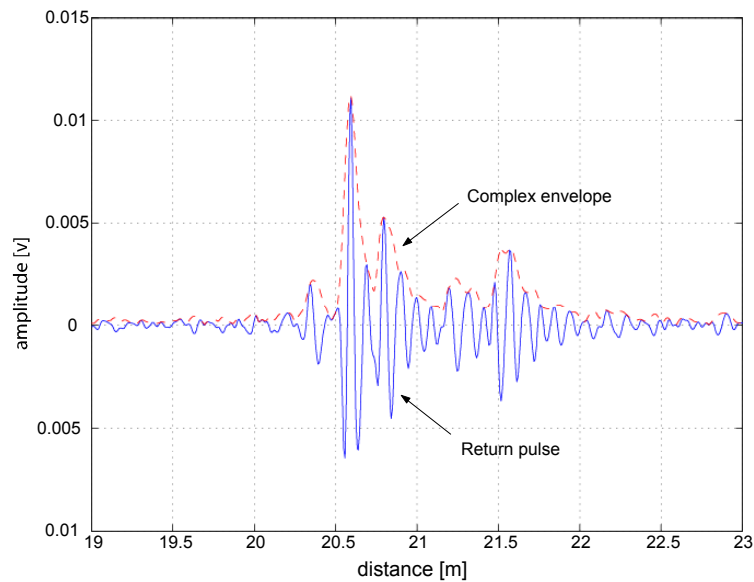
Figure 13. *Comparison of return pulse waveform and its complex envelope (via Hilbert transform).*

Given a real-valued signal waveform *s(t)*, the corresponding *analytic signal* is defined as

$$\psi(t) = s(t) + iH[s(t)], \qquad\qquad (2)$$

where the imaginary component, $H[s(t)]$, is the Hilbert transform of *s(t)*—

$$H[s(t)] = \mathcal{P}\left[\frac{1}{\pi}\int_{-\infty}^{\infty}\frac{s(t')}{t-t'}dt'\right]. \tag{3}$$

As this is an improper integral by virtue of the singularity at $t = t'$, it is expressed in terms of a Cauchy principle value, denoted by the symbol $\mathcal{P}$:

$$\mathcal{P}\left[\frac{1}{\pi}\int_{-\infty}^{\infty}\frac{s(t')}{t-t'}dt'\right] = \frac{1}{\pi}\lim_{\varepsilon \to 0}\left[\int_{-\infty}^{t-\varepsilon}\frac{s(t')}{t-t'}dt' + \int_{t+\varepsilon}^{\infty}\frac{s(t')}{t-t'}dt'\right]. \tag{4}$$

This transform remains entirely within the time domain. Further details regarding the use of Hilbert transforms in SAR image processing are provided in [1].

Figure 14 compares returns from the same target (rotating sphere) at different distances ranging from 14 to 49 meters.
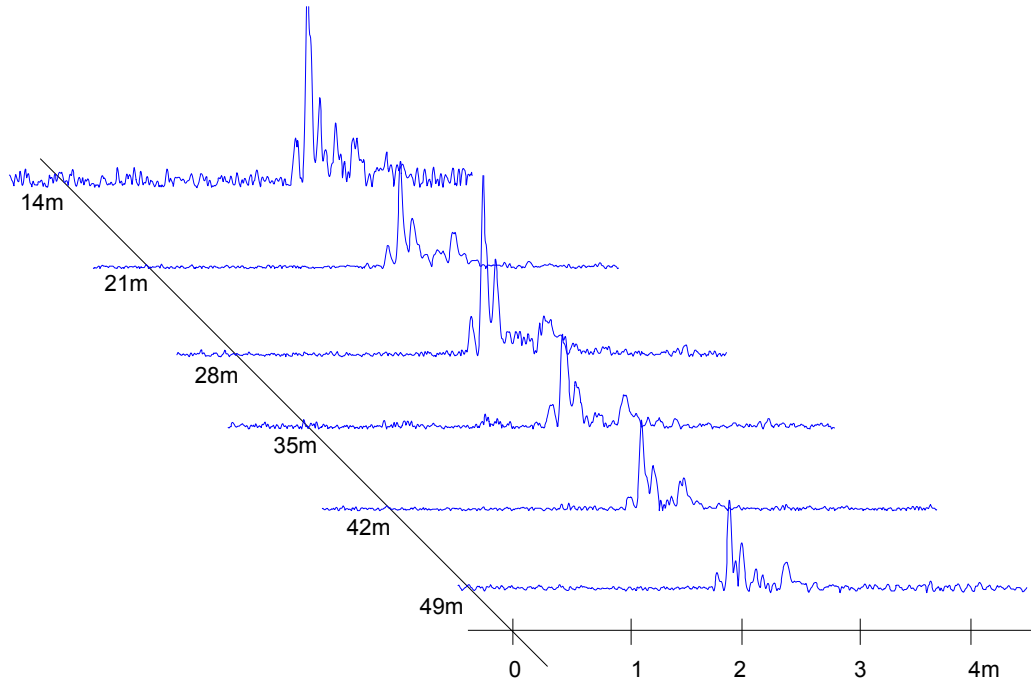
Figure 14. Complex envelope (Hilbert transform) for pulse returns at various target ranges.

4. The impulse radar signal

In contrast with narrowband signals, UWB-SP waveforms are baseband. They are created using impulse generators, and have no explicit carrier frequency. To characterize returns, we can refer to center frequencies and bandwidths, but keep in mind these are controlled only indirectly by variation of pulse width and rise/fall times, which are in turn, hardware dependent.

4.1 Gaussian model

To simplify the analysis, we consider the initial impulse to be in the form of a Gaussian pulse. This is a reasonable assumption based on comparison with a typical pulse obtained directly from the generator[4] (Figure 15)
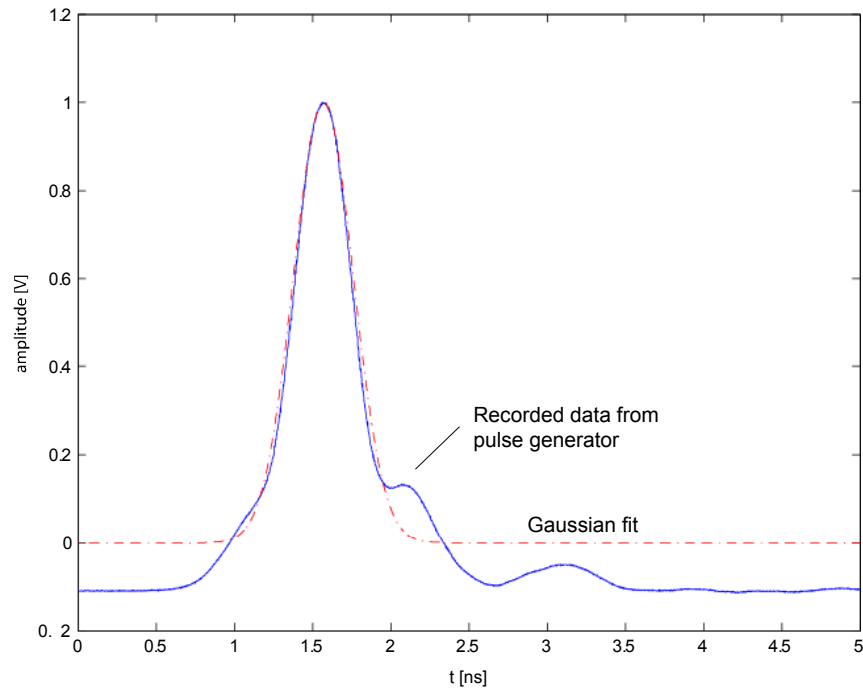
Figure 15. *Measured data (solid line) overlaid with Gaussian pulse (dashed line). FWHM pulse width is τ = 0.42ns.*

---

[4] Avtech Model AVH-HV1-C-T1. This model can output a variable level pulse up to 100 V peak with a width of 600ps. Voltage was attenuated to keep levels within the limits of the oscilloscope. The actual output, taking into account total attenuation and amplitude setting, was 8.6 V.

For this, we have performed a fit on the data, based on a Gaussian distribution

$$f(t) = \frac{1}{\sigma\sqrt{2\pi}} e^{-\frac{(t-t_0)^2}{2\sigma^2}}. \qquad (5)$$

An easily accessible experimental parameter is the full-width at half-maximum (FWHM) pulse width. In the following, we rewrite the Gaussian pulse in terms of the FWHM, τ.

The standard deviation σ and pulse width τ are related by the relation

$$\tau = 2\sigma\sqrt{2Ln2}. \qquad (6)$$

Introducing the parameters $A = \left(\gamma\tau\sqrt{2\pi}\right)^{-1}$ and $\alpha = \left(2\gamma^2\tau^2\right)^{-1}$, along with the scaling $\gamma = \left(2\sqrt{2Ln2}\right)^{-1} \approx 0.42$, we obtain

$$f(t) = Ae^{-\alpha(t-t_0)^2}. \qquad (7)$$

We find that for the measured data in Figure 15, the FWHM pulse width is *0.42ns*. This appears to be an extremely narrow pulse, but recall this was collected directly from the pulse generator, and experienced none of the distorting factors typical of the transmit path.

In choosing a Gaussian form, we lose some flexibility for system parameters, as we cannot independently specify pulse width and rise times. In *narrowband* pulsed radar, rise time is not typically considered and signal bandwidth is defined as *1/Δt*, where *Δt* is the pulse width. As the pulse width decreases however, the rise time becomes a significant fraction of the total pulse width. As rise time decreases, the pulse must comprise higher frequency components.

We can however, use this model to examine pulse returns and to estimate transmitted pulse widths. A previous paper [1] established that target return waveforms could be modeled as Gaussian fourth-order derivatives.

Antenna calibration data is supplied by the manufacturer, Farr Research Inc. [9], in the form of an impulse response *h(t)*, where *$V_{rec}(t) = h(t) * E_{incident}(t)$*. Starting with the Gaussian waveform as the incident pulse, this is convolved with the impulse response of the transmit antenna,

$$p_{Tx}(t) = p * h_{Tx} = \int p(\tau) h_{Tx}(t-\tau)d\tau, \qquad (1)$$

with the result shown in Figure 16a. In turn, this result undergoes a 180° shift to model a simple reflection from a scatterer, and is finally convolved with the receive antenna impulse response to yield Figure 16b.

$$p_{Rx}(t) = -p_{Tx} * h_{Rx} = -\int p_{Tx}(\tau) h_{Rx}(t-\tau)d\tau, \qquad (2)$$
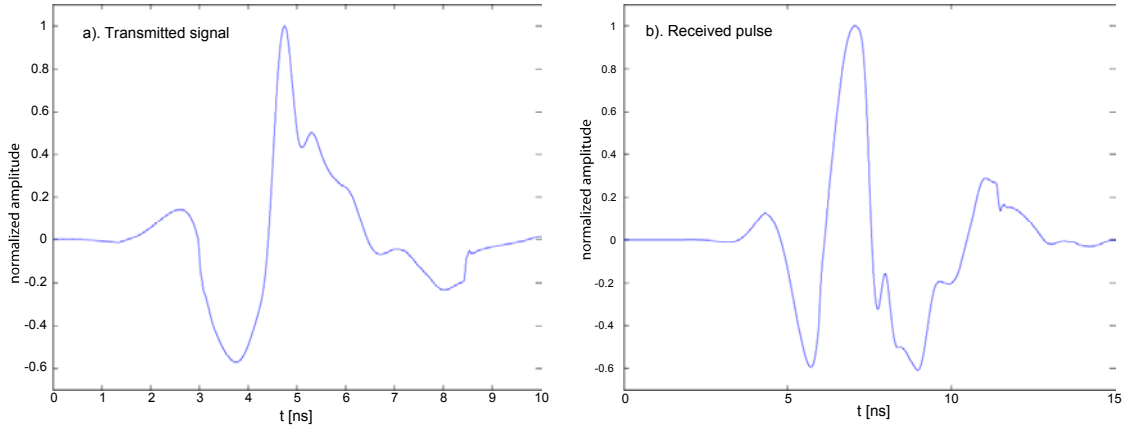
Figure 16. *Predicted Tx and Rx signals resulting from convolution analysis.*

This result can be compared with the target response from measured data as displayed in Figure 17. There is obviously qualitative agreement, although we would not expect an exact match owing to characteristics of the physical environment and the specific target RCS.
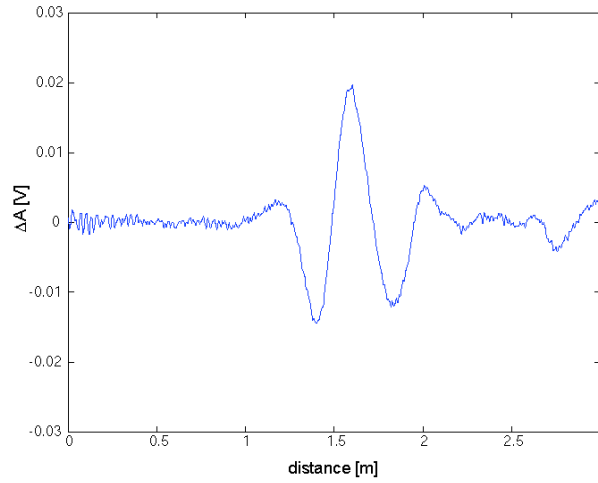
Figure 17. *Target response (measured data)*

Referring back to the expression for *f(t)*, and obtaining the fourth-order derivative,

$$f^{(4)}(t) = A\left(16\alpha^4 t^4 - 48\alpha^3 t^2 + 12\alpha^2\right)e^{-\alpha t^2}, \tag{8}$$

from which we can derive, via the Fourier transform,

$$F^{(4)}(\nu) = 16\pi^4 \nu^4 A \sqrt{\frac{\pi}{\alpha}} e^{-\pi^2 \nu^2 / \alpha}, \tag{9}$$

where the frequency in Hz is denoted ν.

4.2 Model validation

In the following, we compare this model with experiment. Figure 18 shows the time-domain pulse and how it reproduces the shape and duration of experimental data. The only free parameter is τ, the FWHM pulse width of the original Gaussian pulse as in Figure 15.
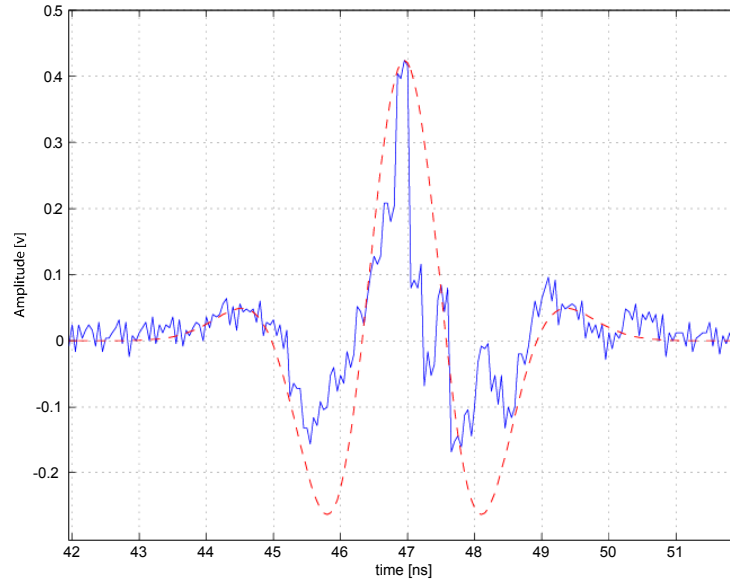
Figure 18. Gaussian 4th order time-domain pulse (dotted line) overlaid on experimental data (τ = 1.3 ns FWHM).

Based on this model, we can obtain an analytic value for the power spectrum. Once again, the agreement with experiment is quite good. The pulse broadening that occurs between the original pulse generator output, τ = 0.42 ns (Figure 15) and the received pulse (FWHM fitted to 1.3 ns, Figure 18) is presumably due to bandwidth limitations of the RF components and sampling. The same effect, with comparable magnitude has been noted elsewhere ([10] and [11]):

- τ = 0.66 ns broadened to 2.5 ns;

- τ = 0.66 ns broadened to 1.44 ns.

As a further comparison between theory and experiment, Figure 19 shows the power spectra corresponding to the time-domain pulse in Figure 18. The red dotted line again refers to theoretical prediction. The match for frequencies under 1GHz is very good, providing more support for the waveform interpretation elaborated on in this report. The spectrum beyond 1GHz is predominantly noise generated.
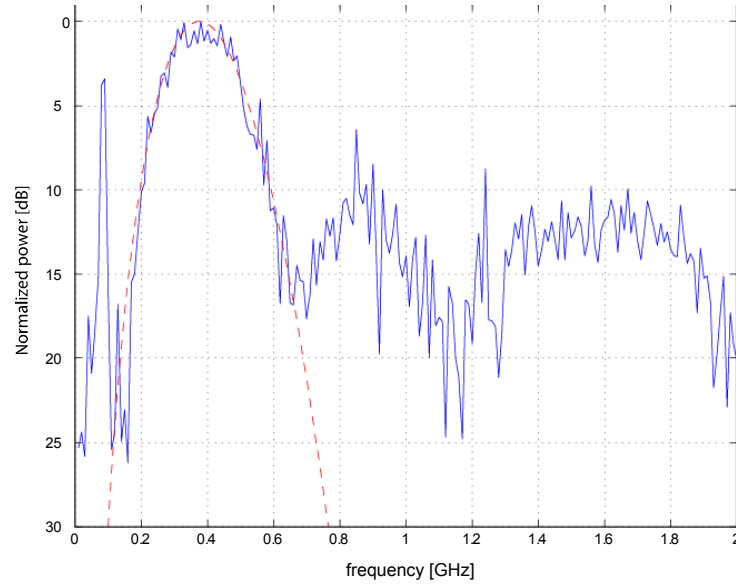
Figure 19. *Gaussian 4th order spectra (dotted line) overlaid on experimental data. Center frequency f_c = 0.38GHz, FWHM$_{3dB}$ = 0.22GHz.*

4.3 Radiation patterns

The standard approach to analyzing radiation patterns is based on transmission of sinusoidal waveforms. This is no longer the case for UWB impulse radar: with no carrier and a narrow pulse width, the signal is distorted as a consequence of transmission. This becomes an important consideration in analysis of waveforms [12].

The electric field intensity at any point is $\vec{E} = -\nabla V - \partial_t \vec{A}$, where V is the electric scalar potential and $\vec{A}$ the magnetic vector potential, defined by $\vec{B} = \nabla \times \vec{A}$ (see for example, [13]). Next, take the time derivative

$$\frac{\partial \vec{B}}{\partial t} = \frac{\partial}{\partial t}\left(\nabla \times \vec{A}\right) = \nabla \times \left(\frac{\partial \vec{A}}{\partial t}\right). \qquad (10)$$

This is substituted into Faraday's law (MKS)

$$\nabla \times \vec{E} = -\frac{\partial \vec{B}}{\partial t} = -\nabla \times \left(\frac{\partial \vec{A}}{\partial t}\right), \qquad (11)$$

which implies $\vec{E} = \partial_t \vec{A}$. In turn, the magnetic vector potential is proportional to current.

From these results, we see that the field components from an electric dipole are proportional to the time-derivative of the current $\dot{I}\left(t^*\right)$, and to the *second* time-derivative of the input voltage $\ddot{V}\left(t^*\right)$. The notation $t^* = t - r/c$ indicates retarded time. Since the operators are linear, the combined operations of transmit and receive will yield the fourth time-derivative as obtained with the Gaussian model.

5. System characterization

The basis of the present study is the radar equation, which relates the received power to various parameters associated with EM propagation and detection. The following analysis uses a realistic parameter set, although the calculations should be interpreted carefully. In specific scenarios, it may be possible to enhance the radar performance beyond the contemplated model [5].

The radar equation below provides the SNR for multiple pulses of power, P_t, as a function of antenna gain, G, wavelength, λ (nominally at the center frequency), target RCS, σ_0, range, R, system losses, L, noise figure, F_n, and bandwidth, B. Boltzmann's constant[5] is denoted by k and T_0 is the reference temperature, 290K. Degradation due to clutter returns is captured with the parameter L_c. The value N denotes the number of pulses integrated to obtain the given SNR.

With these parameters, the signal to noise ratio becomes [14]

$$SNR = \frac{P_t G^2 \lambda^2 \sigma_0 N}{(4\pi)^3 R^4 L F_n k T_0 B L_c} . \tag{12}$$

The theoretical antenna gain is:

$$G = \frac{4\pi A_e}{\lambda^2} , \tag{13}$$

where $A_e = \eta A$ is the effective antenna area. The antenna efficiency is characterized by the parameter η, such that $0 < \eta \le 1$.

The radar power is derived from a pulse voltage of $\sim 10^3$V (peak) at the terminals of a line of characteristic impedance of between 50 and 100 Ω. The antenna gains are based on a dish diameter of about 0.5. The estimated losses comprise 10 dB in the antenna feed and the wideband antenna itself and occur on both transmit and receive. The high bandwidth is obtained by heavy damping designed to broaden antenna response without generating ringing or phase dispersion.

The noise figure includes the effect of noise introduced by the front-end amplifier. The RCS is that of a 0.15 m radius sphere ($\pi r^2 \approx 0.07 m^2$). In practice the returns may be distributed among many resolution cells; for example, if the return is spread over 10 cells, the effective RCS, σ_eff, for any one cell will be $\sigma_{eff} \approx 0.1\sigma_0$. The pulse-integrated SNR predicted by the radar equation is given in the last row of the table, along with the value derived directly from measured data. Table 2 provides a summary of the parameter set.

---

[5] k = 1.38x10^{-23} J/K, or −228.6 dBw/Hz/K.

Table 2. *Radar equation parameters*

Parameter	Value	Symbol	Notes and information source
Peak transmit power [w]	10^4	P_t	Instrument spec
Center frequency [GHz]	0.4	f_c	Experiment / data fitting (see page 21)
Bandwidth [GHz]	2	B	Experiment / data fitting (see page 21)
Wavelength [m]	0.75	λ	Calculated from f_c
Antenna gain [dBi]	14.8	G	Experiment (see page 27)
Antenna efficiency	0.5	η	Estimated (typical – antenna resistively loaded)
Antenna area [m^2]	0.19	A	Measured
RCS [m^2]	0.07	σ_0	$\pi\, r^2_{sphere}$ ($r_{sphere} \sim 0.15$m) Target is metallic sphere
Range [m]	28	R	Measured
System losses [dB]	16	L	Estimated (cable, connector losses)
Clutter [dB]	3	L_c	Estimated (monostatic configuration)
Receiver noise figure [dB]	10	F_n	Instrument spec / estimate (see page 28)
Pulse integration	50	N	Processing parameter
SNR (calculated) [dB]	**43.7**		
SNR (measurement) [dB]	**44.0**		

This parameter set was used to construct a set of SNR vs. Range curves which are in turn, plotted along with a set of discrete data points derived from experiment (refer to Figure 20).
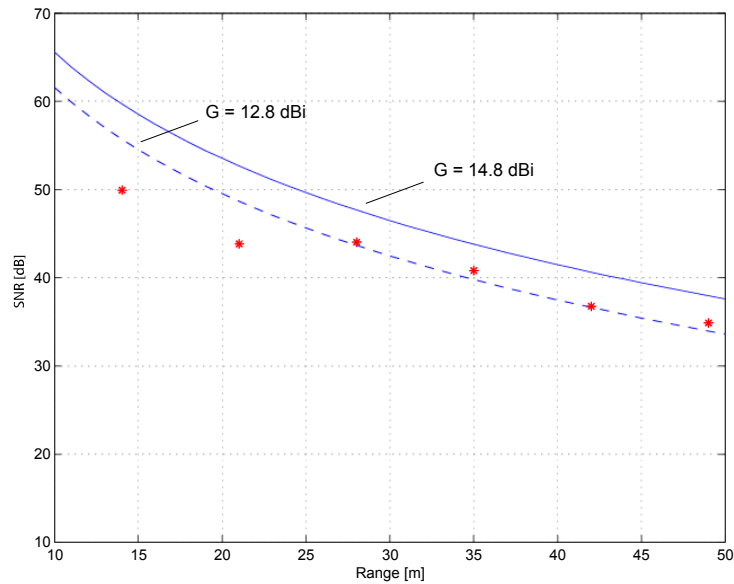
Figure 20. *Predicted SNR vs. Range (solid & dashed curves) compared with experimental results (points).*

There are two curves displayed, for different antenna gains. Because the antenna gain appears as a squared quantity in the range equation, it is a relatively sensitive parameter as can be observed in the plots – the predicted SNR varies across a range of *4dB* for *ΔG = 2dB*. The method for estimating antenna gain is outlined in the next section.

The apparently poor performance of the model at a shorter range can be misleading―it is actually the result of the transmit pulse not being adequately time-gated out, and excessive power gets into the receive antenna. Although the signal strength is good, there is excessive clutter, raising the noise floor. This in turn, artificially lowers the signal to noise ratio.

5.1   Antenna beamwidth and gain

To obtain an estimate of the Farr antenna beamwidth, a set of measurements were taken to record peak amplitude over a range of aspect angles. In what follows, *aspect angle* is defined as that angle existing between the main beam of the transmitting antenna and the main beam of the receive antenna. That is, for one antenna pointed directly at the other, the aspect angle is zero degrees.

Transmit-Receive (TX/Rx) separation remained fixed for each measurement, and the Tx antenna was manually swept through a range of aspect angles from 0˚ to 60˚.

Table 3. *Data for received signal strength vs. aspect angle.*

Aspect angle [degrees]	Receive voltage [mV] (on channel 2)	Gain [dB]
0	522.6	0.0
10	423.7	-1.82
20	291.3	- 5.08
30	242.2	-6.68
40	206.4	-8.07
50	181.6	- 9.18
60	159.2	- 10.32

Transmit voltage recorded on channel 1 was 1.39 V. Assuming a unit resistance, we can calculate the received power at each angle, $P(\theta) = mV \times 10^{-3}/\Omega$. From this, the relative gain is

$$G_{dB}(\theta) = 10 \log_{10}\left(\frac{P}{P_{max}}\right) \quad\quad\quad (14)$$

In Figure 21, these values were fitted to a quadratic function, yielding an approximate value of 26˚ for the 3dB point of the antenna beamwidth.
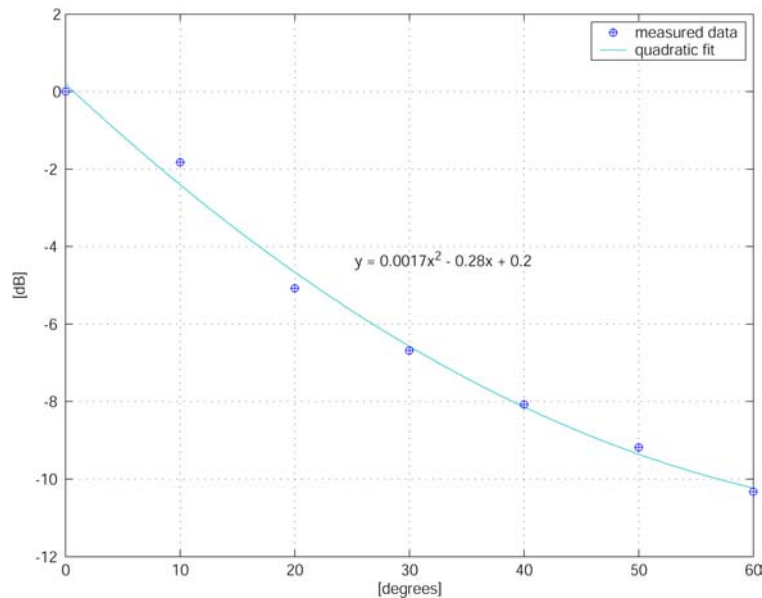
Figure 21. *Antenna gain vs. aspect angle.*

Another way of viewing this information is on a polar plot, (refer to Figure 22) where the beam pattern is more apparent.
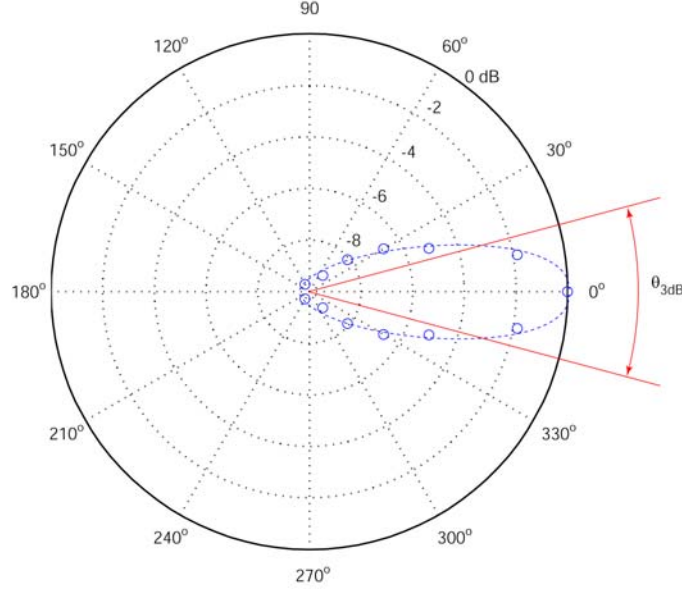
Figure 22. *Polar plot showing experimental antenna beamwidth.*

We can use the measured beamwidth to obtain an estimate of antenna gain. To do so, we first consider the surface area of a sphere,

$$\iint_{surface} d\Omega = \int_0^{2\pi} d\varphi \int_0^{\pi} \sin\theta \, d\theta = 4\pi \,.$$ (15)

Converting from radian, this is $4\pi \times (180/\pi)^2 = 41{,}253$ square degrees. An antenna with 3-dB horizontal and vertical beamwidths of θ_H and θ_V respectively, therefore radiates into $\theta_H \theta_V$ square degrees out of the total surface area. Accounting for an antenna efficiency of η, we have

$$G \approx \frac{41{,}253}{\theta_H \theta_V} \eta \,.$$ (16)

For example, given the symmetry of the Farr antenna under consideration, we expect the horizontal and vertical beamwidths to be equivalent. For the moment, we neglect ground effects. Therefore, $\theta_H = \theta_V = 26°$, and setting $\eta = 0.5$ results in the approximate value $G \approx (41{,}253/26^2)0.5 = 30.5$, or in dB, $G_{dB} \approx 14.8 \, dBi$. Here, *dBi* refers to gain with respect to *isotropic*, an antenna that radiates equally in all directions.

Due to the experimental method, there exists some uncertainty in the beamwidth; the estimated gain should be considered an upper limit until more precise measurements can be made.

5.2   Receiver noise figure

In the series of measurements carried out here, the Tektronix oscilloscope effectively acts as a receiver and detector. As such, it is subject to noise impairments, which we discuss presently.

From the published specifications of the TDS 7404 [15], the highest sensitivity is 2mV/division, resulting in 16mV at full-scale deflection. In turn, the hardware employs an eight-bit digitizer. At a sampling rate of 20GS/s and analog bandwidth of 4GHz, the A/D resolution of the scope is limited to 4.8 effective bits. This means that approximately 3 bits are lost due to quantization noise, jitter, A/D nonlinearity, and interpolation error.

For the full 8-bits (2^8 = 256 levels), we have

16 mV / 256 levels = 0.0625 mV/level.

Allowing 3 bits for noise, (2^3 = 8 levels),

8 * 0.0625 mV/level = 0.5mV.

In the calculation of noise figure this becomes the output voltage. The input signal is given by thermal noise [16]:

$$
\begin{aligned}
V_{rms}^2 &= 4kTBR \\
&= 4\left(1.38 \times 10^{23}\, J/K\right)\left(300K\right)\left(4.0 \times 10^9\, Hz\right)\left(50\Omega\right) \\
&= 3.3 \times 10^{-9} V^2
\end{aligned}
$$

Therefore, the oscilloscope noise figure (NF) is

$$
NF = \frac{\left(0.5mV\right)^2}{V_{rms}^2} = \frac{0.25mV^2}{3.3 \times 10^{-9}\, mV^2} = 75.8 \quad \left(NF_{dB} \approx 19dB\right).
$$

5.3   SNR and path loss

Figure 23 shows some aspects of the transient behaviour. The upper plot is a trace of target range vs. scan (pulse) number – that is, for each pulse transmitted and received, the echoed waveform is analyzed to determine the range associated with the highest return voltage peak. The lower trace shows how the maximum amplitude varies with scan number.

What is interesting about this is how the amplitude drops close to zero for the points corresponding to extremes of the range sinusoid. With a little thought, it becomes obvious that this is due to the fact that radial velocity vanishes at the two extrema and therefore the pulse-

to-pulse subtraction will not produce an appreciable voltage signal (This will be discussed further in Section 6, Velocity processing).
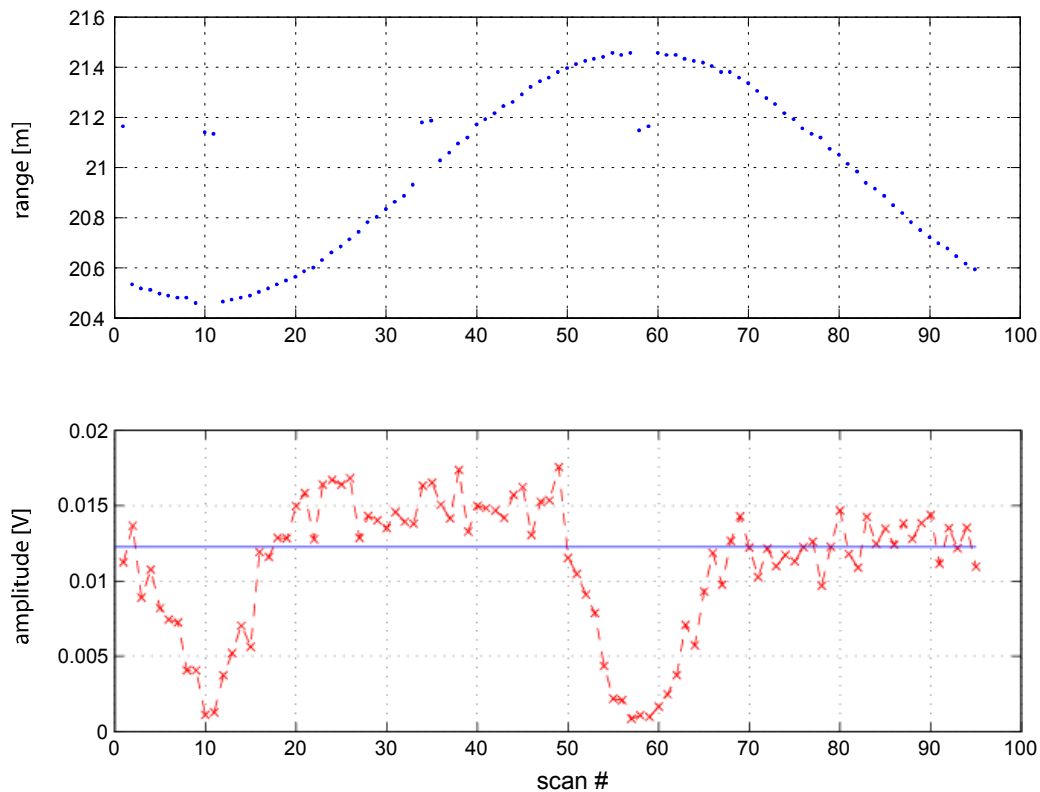
Figure 23. Target range vs. scan number (top), Receive signal peak vs. scan number (bottom).

However, the fluctuating voltage can be used to extract signal power, and in turn, estimate SNR. The lower trace of Figure 23 was averaged to obtain a mean voltage (Indicated by the horizontal line extending across the trace). A more accurate value could be obtained by weighting the average to reduce the influence of the two voltage drops, but this was not carried out.

The results are shown in Table 4, where the SNR over a set of target ranges was determined. The noise power was measured separately.

Table 4. *Calculated return signal power and SNR (N = 50; noise floor = -174 dBw/Hz)*

Range [m]	<V_{rx}> [volts]	Power @ 50Ω [dBw]	SNR [dB]
14	0.0248*	-39.1	49.9
21	0.0123*	-45.2	43.8
28	0.0224	-50.0	44.0
35	0.0155	-53.2	40.8
42	0.0097	-57.3	36.7
49	0.0078	-59.1	34.8

* A 10 dB PAD was placed in the receive path to shield the oscilloscope. Otherwise, signal power received at these distances could damage instrumentation. To get proper voltage, scale by √10 ~ 3.2.

As a means of verifying these results, the received power was plotted vs. range and the path loss exponent determined. As the experimental configuration was essentially free-space propagation, the exponent should be close to 4, as shown in Figure 24. The dashed line shows strict R^{-4} behaviour as comparison (Normalized for 14m reference range).
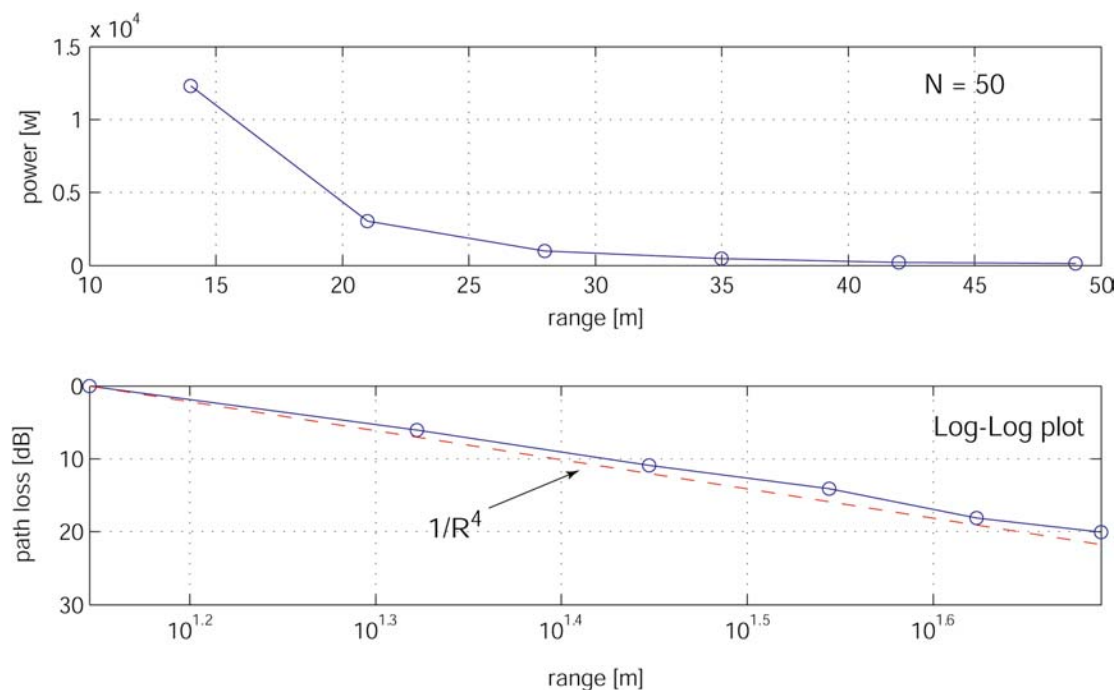
Figure 24. *Received signal power and path loss vs. range to target.*

6. Velocity processing

Traditionally, the processing of moving targets is carried out in the frequency domain with data analyzed in terms of the Doppler shift in frequencies:

$$f_D = \frac{2u}{\lambda},$$ (17)

where f_D is the Doppler frequency with target velocity u. The wavelength of the (narrowband) signal is denoted λ. The principle of operation here is that moving targets can be detected in clutter due to frequency discrimination. Stationary targets will not cause a frequency shift in the carrier.

6.1 Radar imaging

The range processor described in previous sections was modified, yielding a 2D SAR processor. Measurements were carried out, examining the motion of a target rotating about a radius of 0.5m. The use of a sphere as an idealized target ensured a relatively uniform RCS, independent of the point of its orbit.

Radar images for targets at ranges of 7, 21, 35 and 49m are displayed in Figure 25 and Figure 26. Each consists of the reconstructed image and its associated contour diagram. Using the space-time backprojection technique ([1] and [17]), the images clearly show the oscillatory motion of the target, but the signal vanishes as radial velocity approaches zero at the two extremes of motion. Note that motion of the target was slow enough that only one complete rotation was captured for imaging.
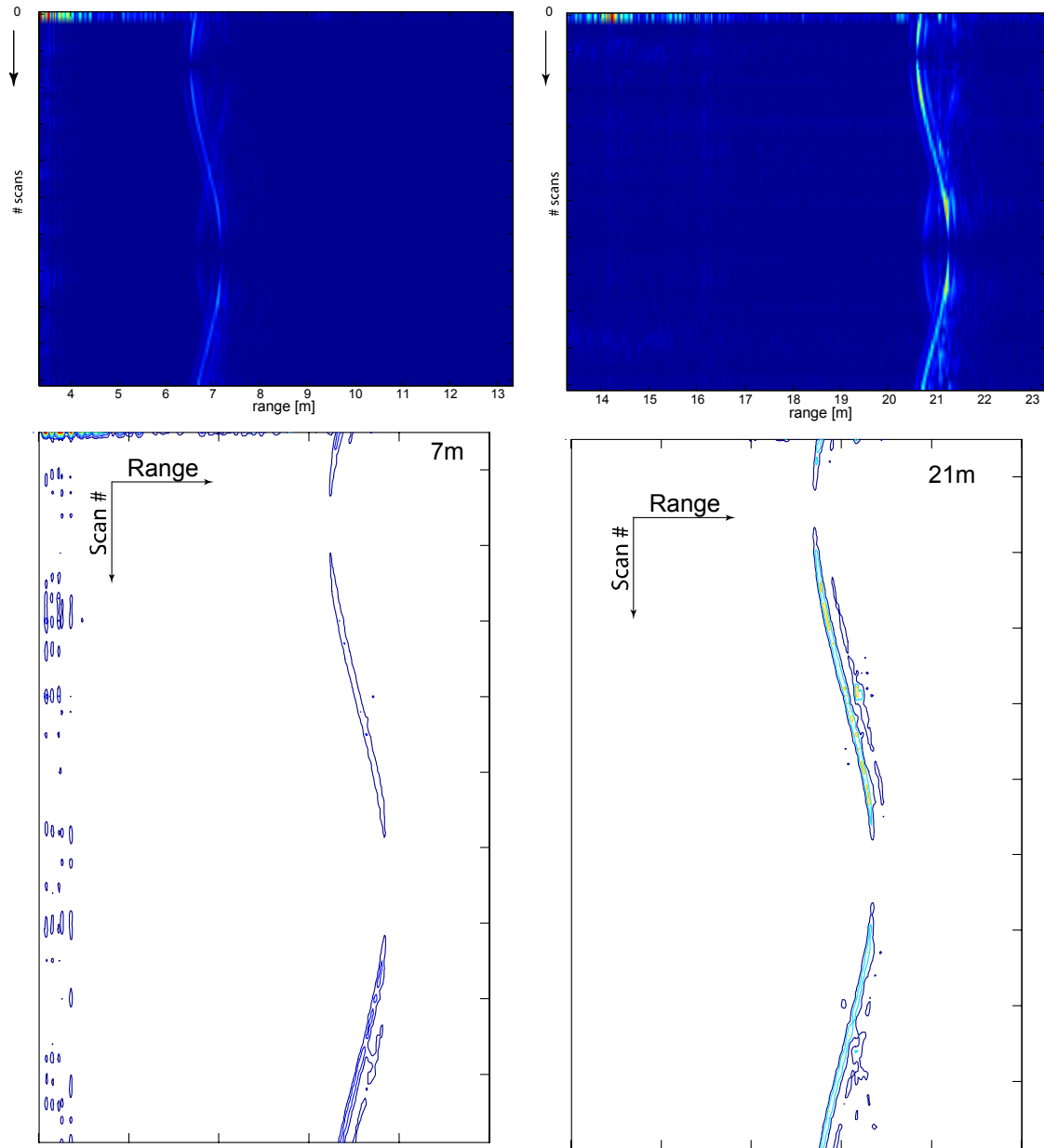
Figure 25. *ISAR images of rotating target at ranges a). 7m and b). 21m.*
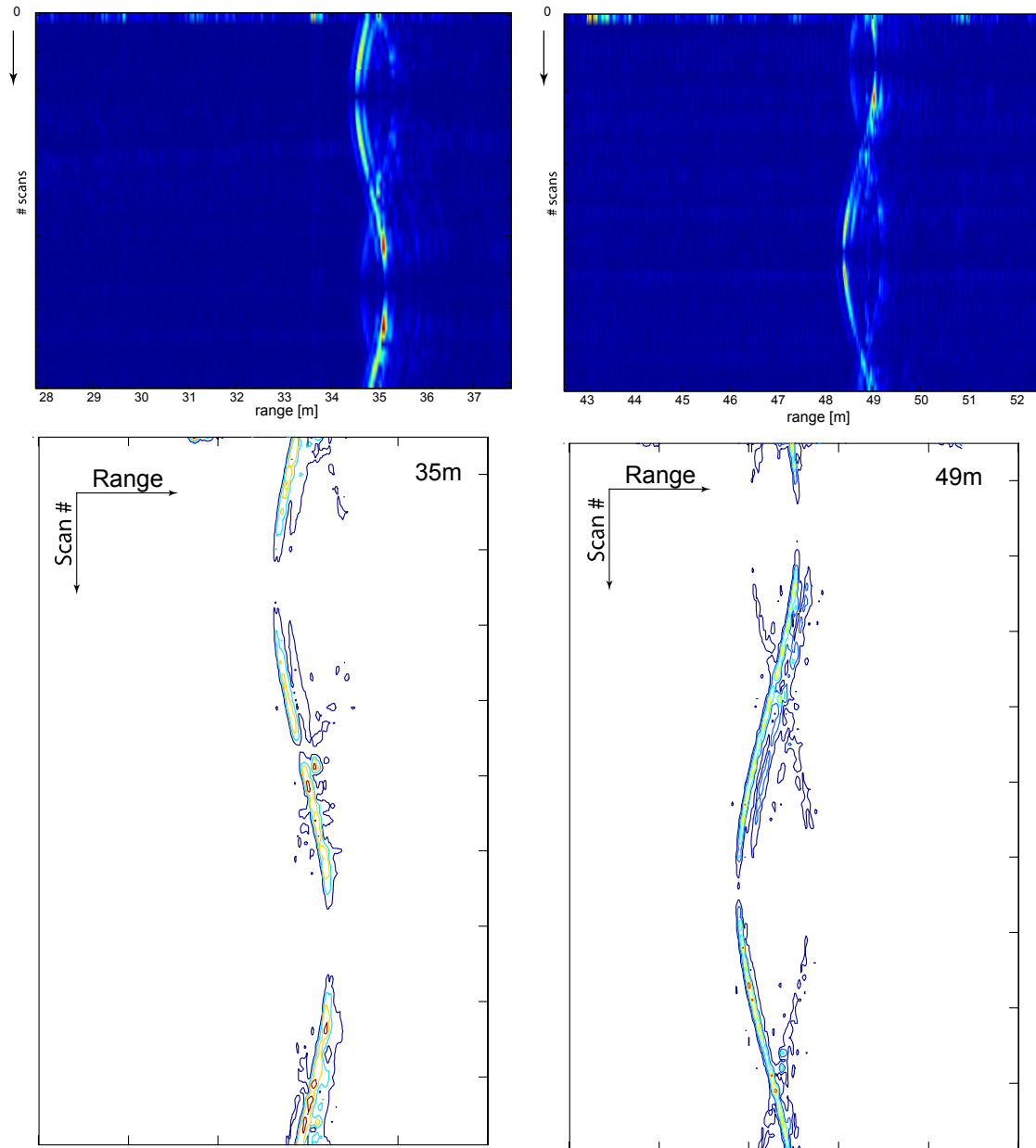
Figure 26. ISAR images of rotating target at ranges a). 35m and b). 49m.

A comparison of contour plots for a target at 21m is shown in Figure 27. The received pulses have been averaged from 20 to 200 data frames. The most obvious trend is that the gap corresponding to near and far extremes tends to widen as the averaging is reduced. This will be discussed further in section 6.2, Non-Doppler MTI.

N = 20   N = 50   N = 100   N = 200
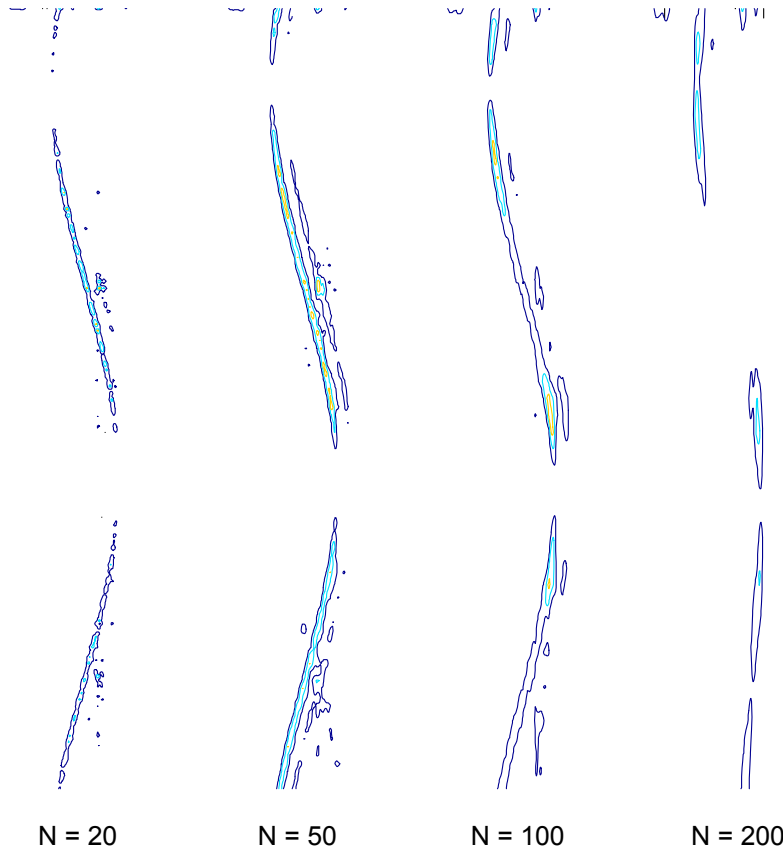
Figure 27. Contour plots for the same target at range = 21m, but with pulses averaged over a number of values of N: 20, 50, 100, and 200.

6.2 Non-Doppler MTI

As indicated previously, UWB-SP radar transmissions are carrier-free and we are unable to exploit Doppler processing. However, target motion is still observable by examining changes in target range from pulse to pulse. The basis for processing now becomes the change in arrival time of the pulse. In effect, we employ a form of *Area Moving Target Indicator (Area MTI)*, comparing the complex envelopes of successive scans to identify target motion.

We consider a target moving at velocity *u*. For a radar transmitting pulses at a PRF equal to *1/T*, the target will move a distance of *uT* for each transmitted pulse. The ensuing time delay is therefore twice the distance moved by the target, divided by the propagation velocity, $\delta = 2d/c = 2uT/c$. Furthermore, when each pulse is transmitted, an echo is subsequently received and sampled at time increments of Δt. In the data studied here, we have $\Delta t = 5.0 \times 10^{-11} s$ (or 50ps). Note that Δt corresponds to a range bin.

To obtain the detectable velocity, we require the target to move at least *k* range bins during the observation time of *N* pulses [18]:

- For velocity u, total distance is NTu.

- For k range bins, the total distance is $k(c\Delta t/2)$

Equating the two, we have

$$u = \frac{kc\Delta t}{2NT} \tag{18}$$

To obtain the *minimum* detectable velocity, we require the target to traverse at least two range bins *(k=2)*. Otherwise, the target is considered stationary.

$$u_{min} = \frac{c\Delta t}{NT} = \frac{c\Delta t}{N} PRF \tag{19}$$

The experimental setup consists of the target centered at $\boldsymbol{R_0}$, rotating with angular velocity ω. The radius of the motion is r. As the target traces out a circular path, the maximum range from the radar is $R_0 + r$ at $\varphi = 0$, while the minimum range is $R_0 - r$ at $\varphi = \pi$ (note that $\varphi = \omega t$).

In general, the range is described by the position vector $\vec{R} = \vec{R}_0 + \vec{r}$, as indicated in Figure 28.
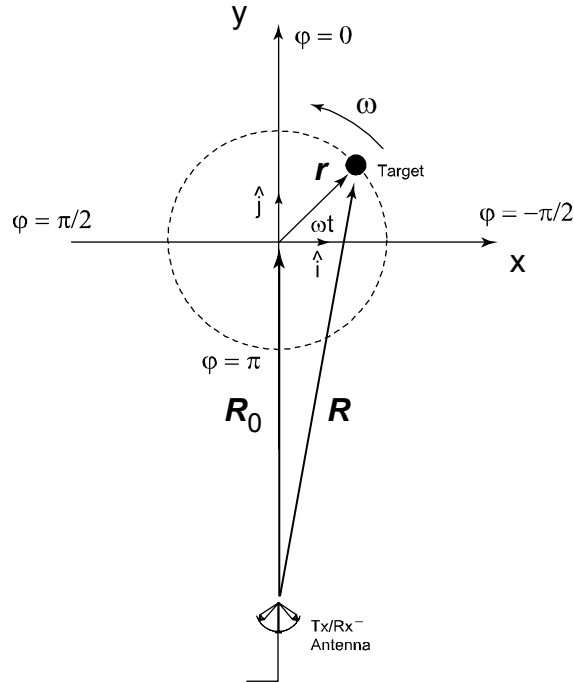
Figure 28. *Configuration for measurement of oscillatory target motion.*
(ω = 1.2 rpm)

Using the law of cosines, we can express the radial distance from antenna to target, R, as a function of φ.

$$R = \sqrt{R_0^2 + r^2 - 2R_0 r \cos(\varphi + \pi)}$$
$$= \sqrt{R_0^2 + r^2 + 2R_0 r \cos(\varphi)}$$

(20)

The radial velocity, in turn, is given by

$$u_{radial} = \frac{dR}{dt} = -\frac{2\omega R_0 r \sin(\varphi)}{2\sqrt{R_0^2 + r^2 + 2R_0 r \cos(\varphi)}}$$

(21)

The maximum velocity occurs at the points $\varphi = \pm \pi/2$, and we have

$$u_{radial}^{max} = \left| \frac{dR}{dt} \right| = \frac{\omega R_0 r}{\sqrt{R_0^2 + r^2}}$$

(22)

This expression is further simplified by making the reasonable assumption that $R_0 \gg r$, which results in $u_{radial}^{max} \approx \omega r$.

To make contact with experimental data, the target executes one rotation about a 0.5m radius every 50s. This is equivalent to an angular velocity of 1.2 rpm, or $\omega = 0.125$ rad/s. The maximum radial velocity is therefore 0.063 m/s. Once we have scaled the displacement (as indicated in Figure 29), we can determine the corresponding velocity (Figure 30).
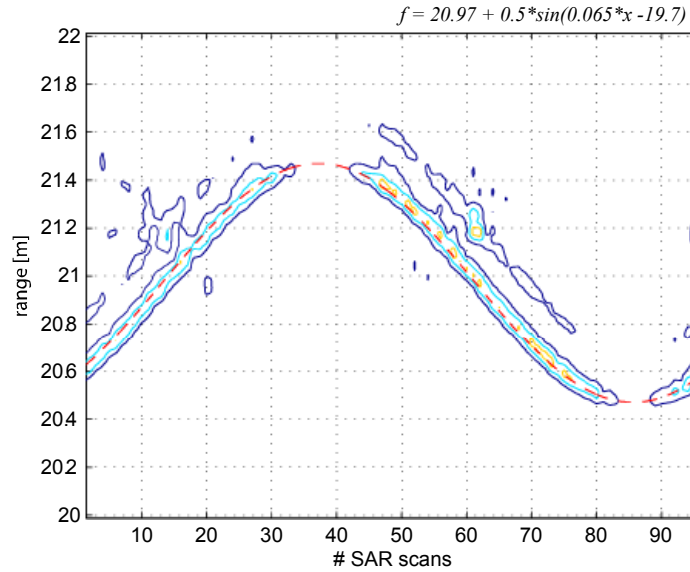
Figure 29. *Experimental data and parametric fit used to extract minimum velocity threshold.*
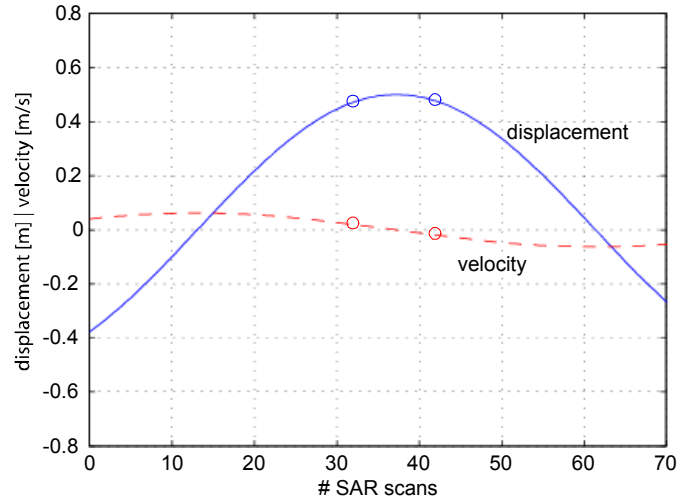
Figure 30. Displacement end points mapped onto radial velocity function.

In this particular example, the PRF is 100Hz, and the number of pulses integrated, *N = 50*. From the expressions developed previously, we have for the minimum detectable velocity —

$$v_{min} = c\Delta t \, PRF \, / \, N$$
$$= \frac{\left(2.998 \times 10^8 \, m/s\right)\left(5.0 \times 10^{-11} \, s\right)\left(100 Hz\right)}{50} \approx 0.029 \, m/s$$

Figure 31 compares theoretical values with those obtained from processed images. While the trend follows theory, there is a discrepancy at lower pulse averaging. This is presumably a result of the increased variance for low averaging and the resulting error in determining the threshold value.
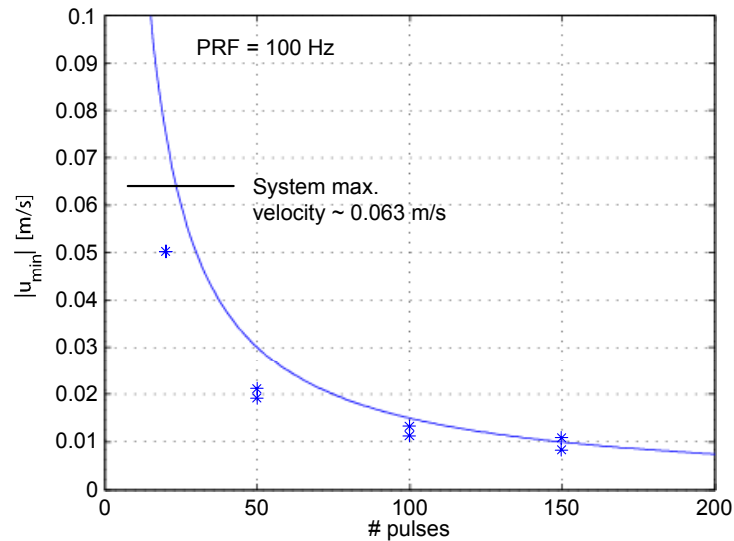
Figure 31. Minimum detectable target velocity as a function of PRF and # averages.

7.   Wall penetration losses

As concrete was selected to be the building material of interest for this project, we need to determine the effects of moisture content on signal propagation and attenuation.

7.1   Wall construction

The materials used in this experiment were standard concrete blocks of approximate dimensions 20 x 20 x 40 cm, with two air pockets inside. Recent studies, [19] and [20], report that dry, solid concrete exhibits a dielectric constant of 8 to 12. The presence of air gaps in the blocks will tend to reduce that value. However, to our knowledge, little has been mentioned in the literature regarding moisture content and to what extent it will increase attenuation.

A concrete block wall as depicted in Figure 32 was constructed to obtain transmission loss data. The transmit antenna was moved from 2 ft. to 5 ft. (60 to 152cm) in two-inch increments (5cm), while the receive antenna remained fixed at a distance of 2 ft. (60cm) from the wall. From this, we were able to obtain a set of closely spaced transmission data over a range of approximately six wavelengths.
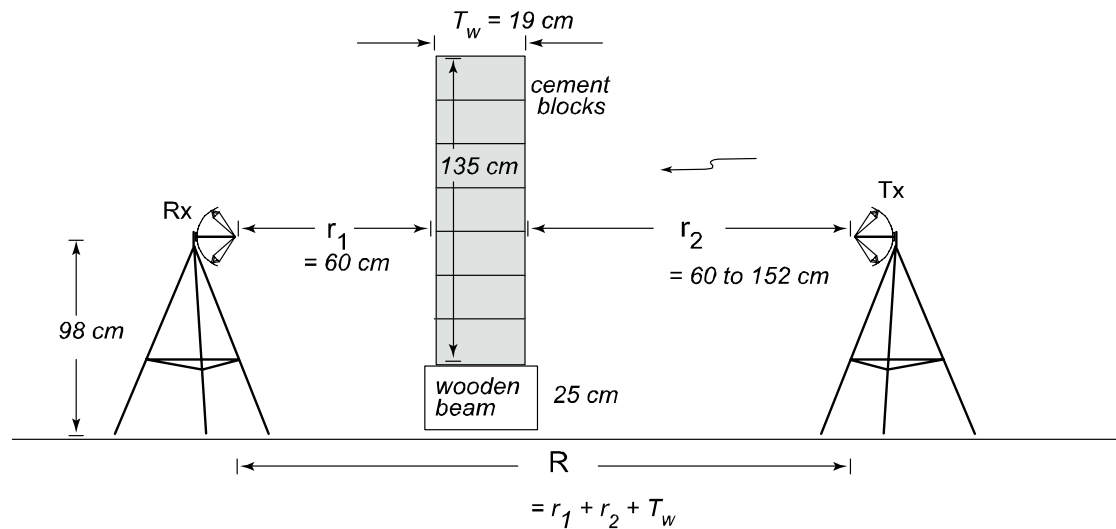
Figure 32. Receive/Transmit configuration for measurements (side view).

The wall dimensions are 53" x 74.75" x 7.5" (135 x 190 x 19 cm). With an antenna height of 98 cm and beamwidth of approximately 26°, there should be minimal direct signal power around the wall and limited diffraction phenomena. In fact, the transmit antenna would need to be moved about nine feet from the wall before leakage of this sort became a factor.

7.2 Data collection

Following this, three sets of measurements were taken:

1. *dry/damp bricks* ― Bricks were stored outside subject to both ambient temperature and climate. The bricks were not visibly wet, but will exhibit typical moisture content. No attempt was made to prepare a reference set of oven-baked dry bricks.

2. *wet bricks* ― Bricks were thoroughly soaked by repeatedly hosing the wall down. Water was applied before each measurement to ensure uniform results. This should provide an upper bound on the degree of attenuation due to water.

3. *line of sight (LOS)* ― The wall was removed, and LOS "free-space" measurements taken to provide a reference.

A diagram of the experimental configuration appears in Figure 33.
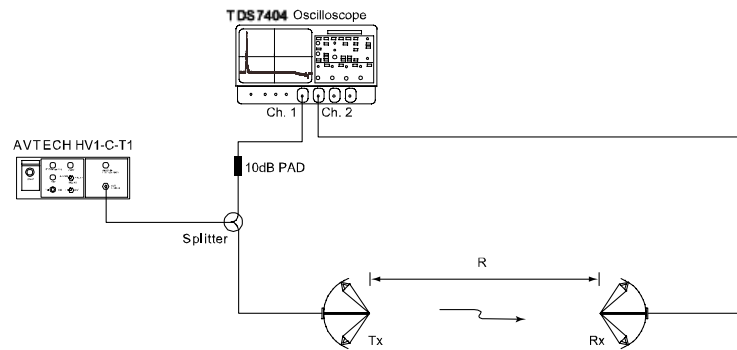
Figure 33. *Experimental configuration*

Dividing through-wall values with the corresponding LOS values produces normalized measurements, eliminating the effect of $1/r^2$ spreading losses, leaving only wall attenuation loss. A typical set of raw data is shown in Figure 34.
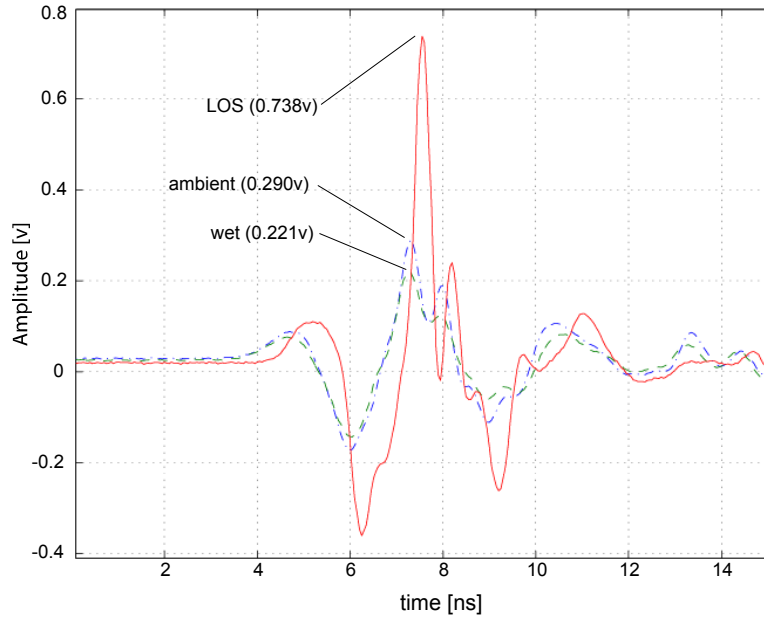
Figure 34. Unprocessed data from wall attenuation measurements (@ 1.36λ).

Tabulating the data as collected in Figure 34, recording only peak values as a function of distance from the wall, the path loss due to line of sight (LOS), and for both dry and wet cindercrete blocks is depicted graphically in Figure 35
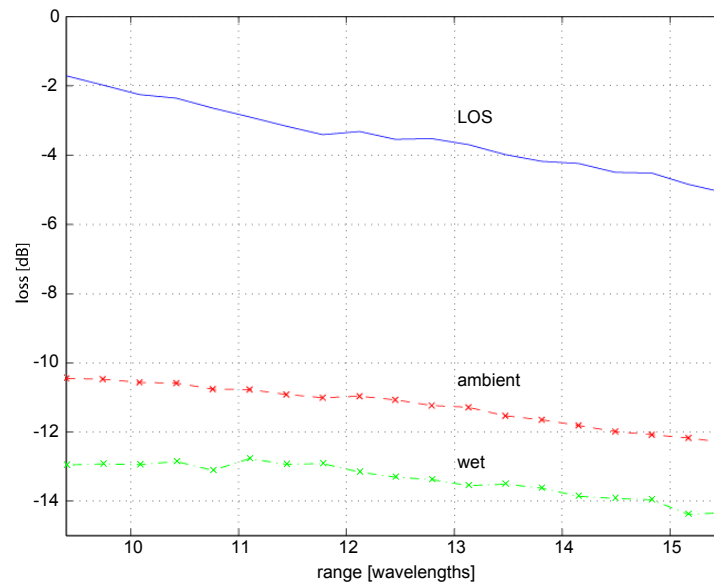
Figure 35. One-way propagation loss, unnormalized.

Figure 36 shows values corrected for free-space path loss. These results show that over a range of about six wavelengths the through-wall losses are between 7 to 9 dB for ambient blocks and between 9 to 11 dB for wet blocks.
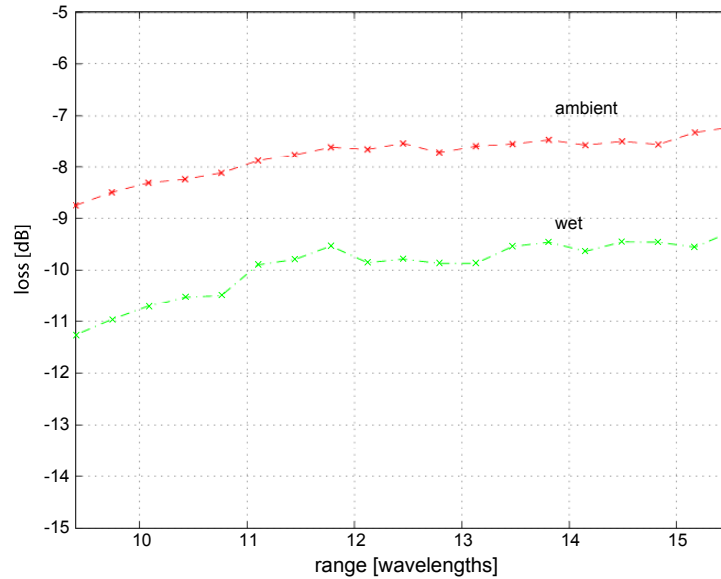
Figure 36. Corrected losses for wall attenuation (one-way).

There is a slight upward trend in the data that seemingly indicates wall attenuation decreases with distance. A possible explanation for this is that as the transmit antenna is moved farther away from the wall, a portion of the energy "leaks" around, either by diffraction or some multipath configuration that bypasses the attenuation of the wall material itself.

Note that this is a systematic effect, which can be verified by considering the differential loss between ambient and wet blocks (see Figure 37) is relatively flat. The average loss calculated from this is $\Delta_{loss} = -2.16 \pm 0.19\, dB$, with a slope of 0.07 ± 0.02 dB/λ.
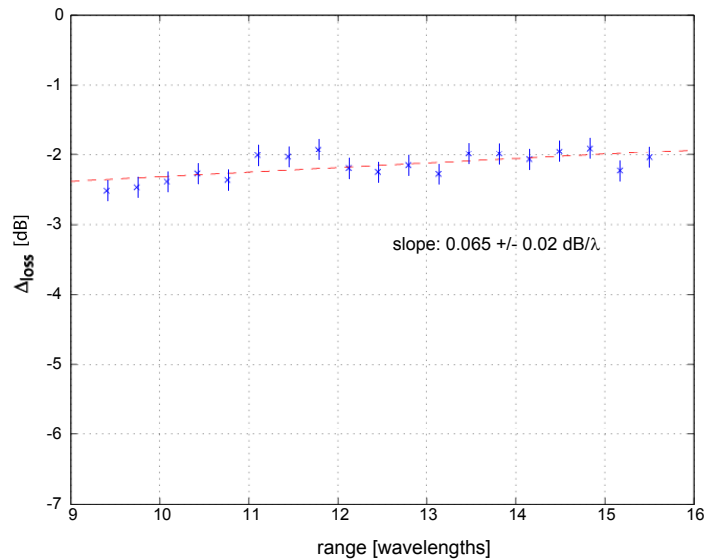
Figure 37. Differential losses for wall attenuation (one-way) due to water film.

7.3 Wall reflections and waveform structure

Part of the loss incurred when transmitting a signal through a wall is due to reflections at the air-dielectric interface. The ratio of transmitted and reflected signal energy is given by the Fresnel equations [21]. These can be expressed in quite general terms for both electric and magnetic fields, and for perpendicular and parallel field orientation. For the purposes of this report, it is sufficient to consider the more restricted case of normal incidence.

We consider perfect dielectrics, where conductivity is neglected ($\sigma \approx 0$); all materials are non-magnetic so that the permeability is unity ($\mu = 1$). Under these conditions the refractive index takes the form $n_i \approx \sqrt{\varepsilon_i}$, where the subscript i denotes either an air or dielectric medium.

It is convenient to make calculations in terms of power, where

$$\rho = \left| \frac{n_2 - n_1}{n_1 + n_2} \right|^2 \tag{23}$$

is the fraction of reflected incident power. The transmission coefficient, from conservation of energy, is $\tau = 1 - \rho$. Power losses are often expressed in dB:

$$L_\rho = 20 \log_{10} \left| \frac{n_1 - n_2}{n_1 + n_2} \right| \tag{24}$$

and

$$L_\tau = 20 \log_{10} \left| \frac{2 n_2}{n_1 + n_2} \right|. \tag{25}$$

Consider Figure 38, depicting the one-way transmission of a signal through a wall with relative dielectric constant ε_2. The relative dielectric constant of air, ε_1, is approximately one.

— For an incident signal of power P_i, the power transmitted across the first interface into the medium is $P_m = \tau P_i$ (watts).

— In terms of dB, this is $P_{m,dBm} = P_{i,dBm} + L_{\tau,dB}$, where dBm is a convenient measure of power with respect to one milliwatt[6].

— The power returned from the initial wall reflection is $P_{r1} = \rho P_i$ (or $P_{r1,dBm} = P_{i,dBm} + L_{\rho,dB}$).

---

[6] There is a "bookkeeping" issue here. L is a negative quantity, so we unintuitively *add* the loss.

— The secondary reflection is calculated $P_{r2} = \rho(\tau P_i)$, or $P_{r2,dBm} = P_{i,dBm} + L_{\tau,dB} + L_{\rho,dB}$, in dB.

— Finally, the power available to penetrate the wall is $P_m = \tau^2 P_i$ (or $P_{m,dBm} = P_{i,dBm} + 2L_{\tau,dB}$).
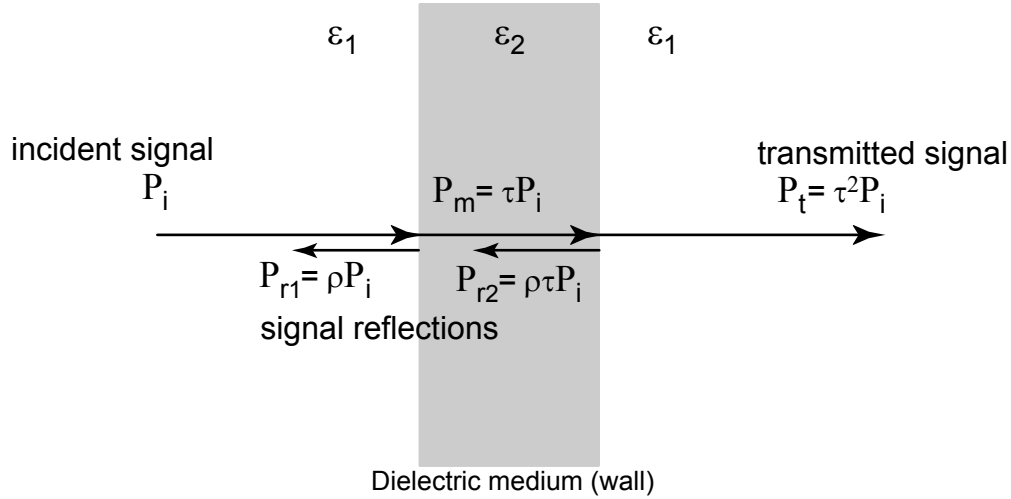
Figure 38. Schematic of reflection and transmission coefficients.

Numerical example: Consider an initial pulse power P_i of 1watt (30dBm), with $\varepsilon_1 = 1$ and $\varepsilon_2 = 10$. This results in $n_1 = 1$ and $n_2 = 3.16$. Therefore, $\rho = 0.269$ and $\tau = (1 - \rho) = 0.73$. The associated *dB* loses are $L_\rho = -5.70$ and $L_\tau = -1.37$.

Table 5. Reflection losses–numerical example.

Quantity	power [watts]	Power [dBm]
Initial power, P_i	1 w	30 dBm
1st reflection, P_{r1}	ρP_i = 0.269 x P_i = 0.269w	$P_i + L_\rho$ = 30dBm – 5.7dB = 24.3dBm
Power in medium, P_m	τP_i = 0.73 x P_i = 0.73w	$P_i + L_\tau$ = 30dBm – 1.37dB = 28.6dBm
2nd reflection, P_{r2}	$\rho P_m = \rho \tau P_i$ = 0.269 x 0.73 = 0.196w	$P_i + L_\rho + L_\tau$ = 30dBm – 5.7dB – 1.37dB = 22.9dBm
Transmitted power, P_t	$\tau P_m = \tau^2 P_i$ = 0.73^2 x P_i = 0.532w	$P_i + 2L_\tau$ = 30dBm – 2 x 1.37dB = 27.26dBm

This results in an overall reflection loss of 2.7dB for one-way transmission through the wall. Note there were a number of simplifications to obtain this value. First, we considered a solid, homogeneous dielectric rather than the cindercrete wall containing air pockets. Second, no wall attenuation was accounted for. This would have come about by having a complex dielectric $\varepsilon = \varepsilon' - i\sigma/\omega\varepsilon_0$, where σ is the conductivity and ω the frequency. The dielectric constant, $\varepsilon_0 = 8.854 \times 10^{-12}\, F/m$.

A closer examination of reflections as the signal reaches a discontinuity provides information about the structure of the received waveform. For example, Figure 39 follows the path of a pulse in time as it passes through a wall, reflecting off of a target.
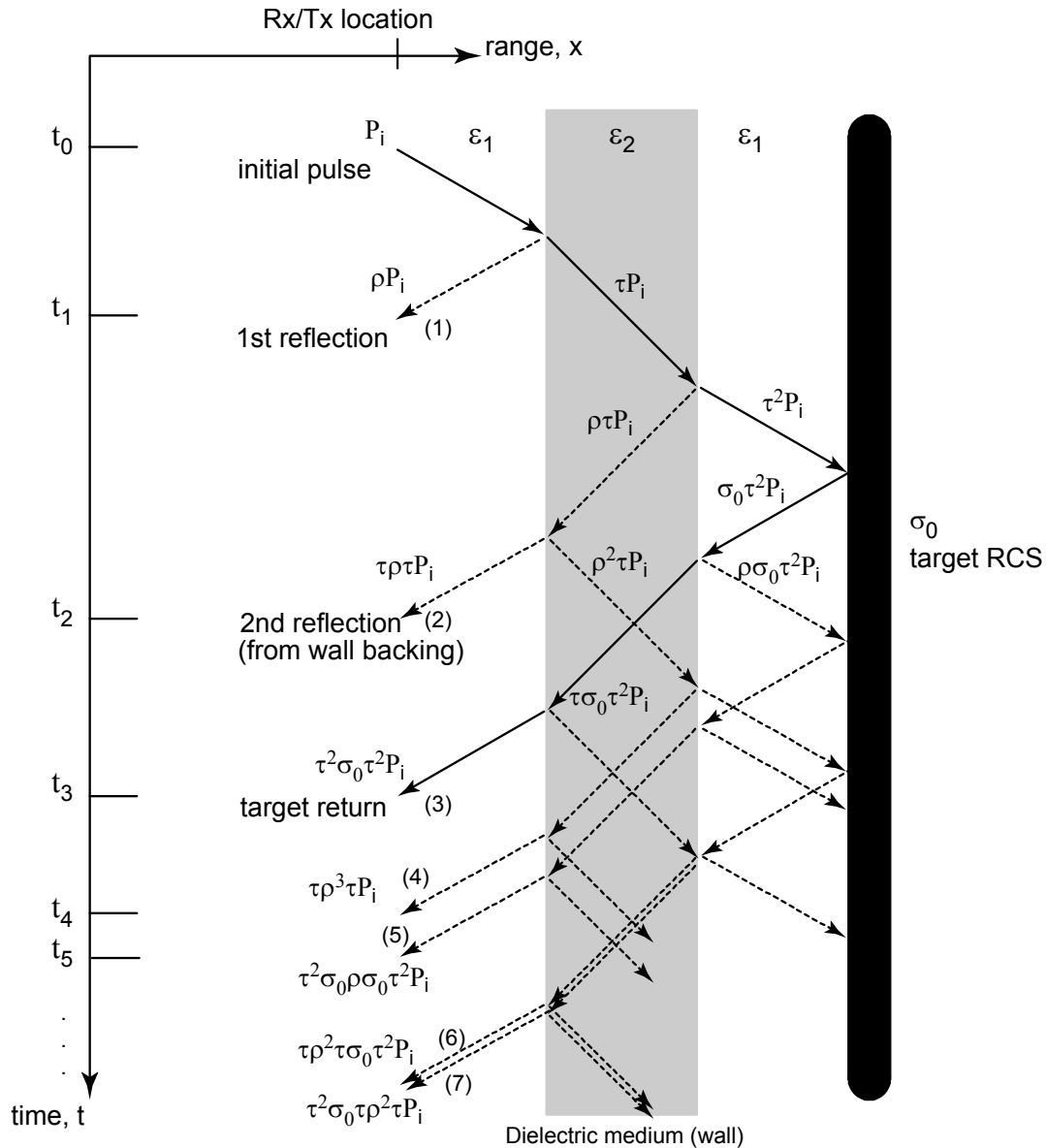
Figure 39. Time-space diagram showing signal propagation through dielectric material (Not to scale).

Moving from top to bottom, the time delay of the received signal increases. Anything fixed in space such as the wall or a stationary target traces out a vertical strip as shown. The lines with arrows show the various paths that can be taken, where the line slope indicates velocity—EM waves moving into the dielectric slow down. In principle, there will be an infinite number of reflections, but since higher orders are severely attenuated, we only consider the first few returns. The reflection and transmission losses are indicated on the diagram similar to that of Figure 38.

A more accurate representation of the time dependence comes from properly accounting for propagation distances and velocity. This was carried out numerically, and the signal power vs. time delay is shown in Figure 40. Note the order in which pulses were received differs from what is indicated in Figure 39. This is expected since that diagram was only used to track the topology of paths and derive terms such as, $\tau^2 \sigma_0 \rho \sigma_0 \tau^2 P_i$. The time and range scales in Figure 39 were altered simply to display the path information more clearly.
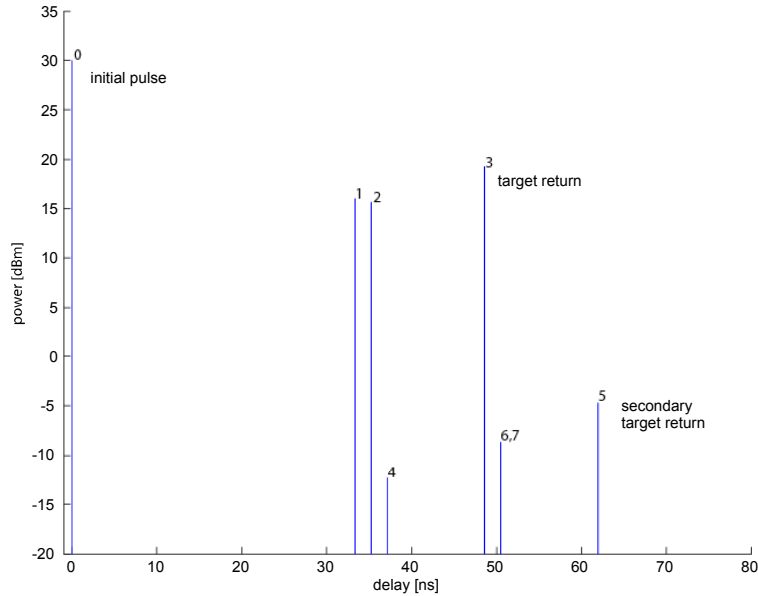
Figure 40. *Time delay vs signal power after multiple reflections from a dielectric wall. Numbered labels refer to return paths as indicated in Figure 39.*

This is an useful result as it shows the relative effects of reflection losses and propagation delays and how they affect the overall waveform shape and attendant pulse shifting due to through wall propagation. This provides a relatively easy and quick way to investigate the influence of dielectric constant and the target RCS. This configuration is for the monostatic case, but could be modified to examine bistatic situations.

8. Wall Clutter

As discussed in the previous section, building materials act sources for multiple reflections. In through-wall imaging applications, this becomes an important factor for image quality. Here, we consider a wall, with a characteristic RCS, σ_0. As the wall is an extended structure and not a point scatterer, it is convenient to express the RCS per unit area of the surface as $\sigma^0 = \sigma_0/A$. The symbol σ^0 is referred to as the normalized RCS, or backscatter coefficient.

The magnitude of σ^0 is strongly dependent on the angle of incidence. The range of incident angles expected for through-wall application is relatively small, and the limiting case of zero incidence angle will be the dominant source of clutter returns. If the wall were to reflect isotropically, then σ^0 would be unity. With isotropic reflection in the half-space, σ^0 becomes 2 (3dB). A relatively smooth surface (Rayleigh criterion) exhibits a strong specular reflection ($\sigma^0 > 2$), and is dominant for normal incidence [22].

8.1 Signal-to-Clutter ratio

The following treatment is adapted from some of the literature in altimeter radar [23]. To examine the signal-to-clutter ratio, we consider the received power from a target of RCS σ_{tgt}, and an arbitrary extended structure with RCS σ_c, where the subscript denotes "clutter". From the standard radar equation, we write the signal S, and clutter C, received powers as

$$S = \frac{P_T G A_e \sigma_{tgt}}{(4\pi)^3 R^4} \qquad (26)$$

$$C = \frac{P_T G A_e \sigma_c}{(4\pi)^3 R^4} \qquad (27)$$

respectively, where A_e is the effective area of the radar antenna. Substituting $\sigma^0 = \sigma_c/A_c$, the signal-to-clutter ratio is

$$\frac{S}{C} = \frac{\sigma_{tgt}}{\sigma_c} = \frac{\sigma_{tgt}}{A_c \sigma^0} \qquad (28)$$

The value A_c is the area of the radar resolution cell and depends on the antenna beamwidth and range. We consider nearly perpendicular incidence angle, and the instantaneous field of view, or illumination area, is easily obtained. Generally, an antenna is characterized by its horizontal and vertical beamwidths θ_H, θ_V, but assuming azimuthal symmetry yields $\theta_H = \theta_V = \theta_{3dB}$. At range R, such an antenna will illuminate an area of diameter D as detailed in the following diagram:

wall cross-section
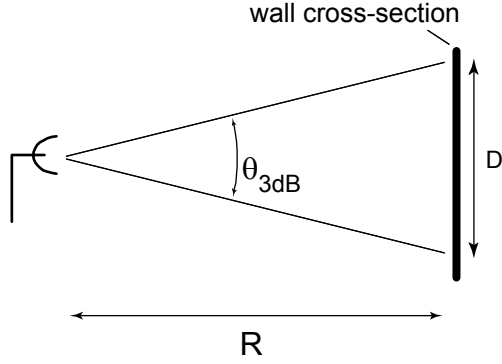
$$\tan\left(\frac{\theta_{3dB}}{2}\right) = \frac{D/2}{R}$$

$$D = 2R\tan\left(\frac{\theta_{3dB}}{2}\right)$$

$$\approx R\theta_{3dB}$$

The area illuminated is therefore $A_c = \pi(D/2)^2 = \pi R^2 \theta_{3dB}^2 / 4$, and the resulting signal to clutter (S/C) ratio is

$$\frac{S}{C} = \frac{\sigma_{tgt}}{A_c \sigma^0} = \frac{4\sigma_{tgt}}{\pi R^2 \theta_{3dB}^2 \sigma^0} \,. \tag{29}$$

Note that the range dependence scales as $1/R^2$ rather than $1/R^4$ as in the noise-limited case. Also, the transmit power P_T does not appear explicitly although it remains an important parameter: increased transmit power increases the received signal, but with a simultaneous increase to clutter power, yielding no overall improvement.

8.2   Transient response

We next wish to determine the power returned from an area element of the wall. Rather than simply examining a point scattering process, we integrate all area elements providing returns at the same instant. There are three factors that affect this–the relative geometry between radar and scattering surface, the antenna pattern on the wall surface, and the signal duration.

For the purpose of this analysis, the geometry remains rather simple. The source of clutter is a flat surface at a distance R from the antenna. The antenna pattern is represented by an angle-dependent gain, $G(\theta)$. Referring to the experimental pattern (Figure 22), a plausible functional form is $G(\theta) = G(0)\cos^a \theta$, where the parameter a controls antenna beamwidth–the larger the value, the narrower the beam. The pulse duration is denoted τ.

Further, we consider the backscatter coefficient to be of the form $\sigma^0(\theta) = \sigma^0(0)\cos^b \theta$. The parameter b adjusts surface roughness (for a smooth surface, b is large).

The received power becomes

$$P_R = \frac{P_T G^2(\theta)\lambda^2 \sigma^0(\theta)}{(4\pi)^3 R^4} \,. \tag{30}$$

We next determine how the received power changes in time given that both the antenna pattern and backscattering coefficient display an angular dependence. The time interval is limited to small multiples of the pulse width, say 10τ. For an infinitesimal area of radius z and width dz, at time t we have (refer to Figure 41)

$$
\begin{aligned}
P_R(t) &= \int_0^{z_t} P_R\, 2\pi z\, dz \\
&= \frac{2\pi P_T \lambda^2}{(4\pi)^3} \int_0^{z_t} \frac{G^2(\theta)\sigma^0(\theta)}{R^4} z\, dz \\
&= \frac{2\pi P_T \lambda^2}{(4\pi)^3} \int_0^{z_t} \frac{\left(G(0)\cos^a \theta\right)^2 \left(\sigma^0(0)\cos^b \theta\right)}{R^4} z\, dz \\
&= \frac{P_T \lambda^2 G^2(0)\sigma^0(0)}{32\pi^2} \int_0^{z_t} \frac{\cos^{2a+b}\theta}{R^4} z\, dz
\end{aligned}
\tag{31}
$$
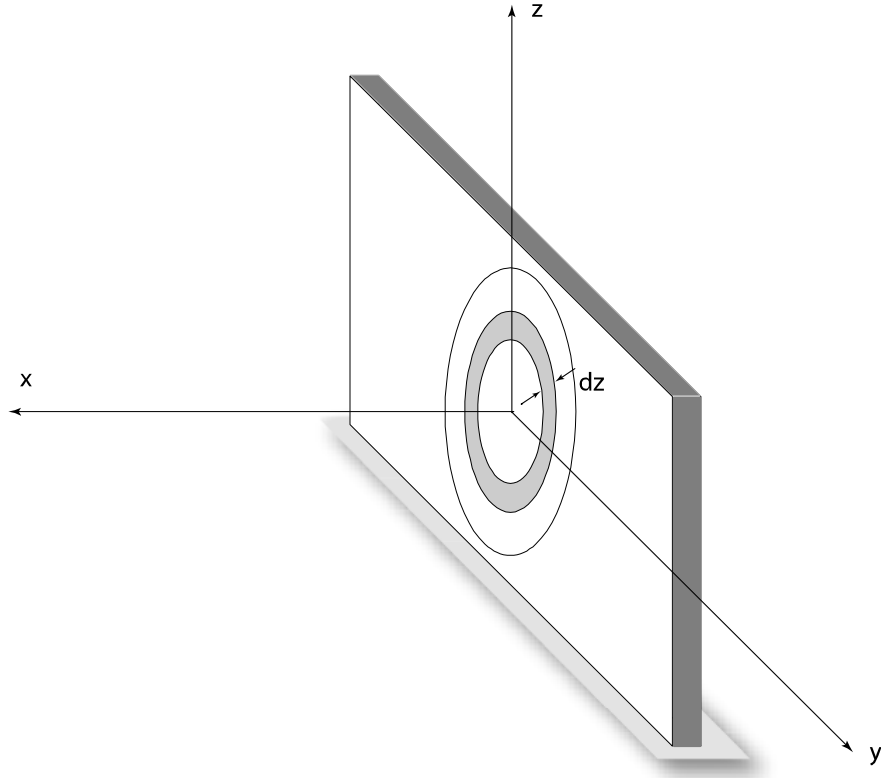
Figure 41. *Geometry used to calculate clutter pulse returns.*

Even though we consider normal incidence, there still exists a narrow range of angles over which the pulse interacts with the wall. The first task therefore, is to relate the incident angle, θ to the radius of the illuminated area, z. In the following diagram, distance perpendicular to

the wall is denoted R_0 (at time $t = 0$). At a later time t, the area of illumination has increased, along with the propagation delay, which is now $ct/2$. The radius of the illumination disk is z_t.

$$R = R_0 + \frac{ct}{2}$$

$$R^2 = R_0^2 + z_t^2$$

$$\left(R_0 + \frac{ct}{2}\right)^2 = R_0^2 + z_t^2$$

$$\Rightarrow z_t^2 = ctR_0 + \frac{c^2 t^2}{4}$$
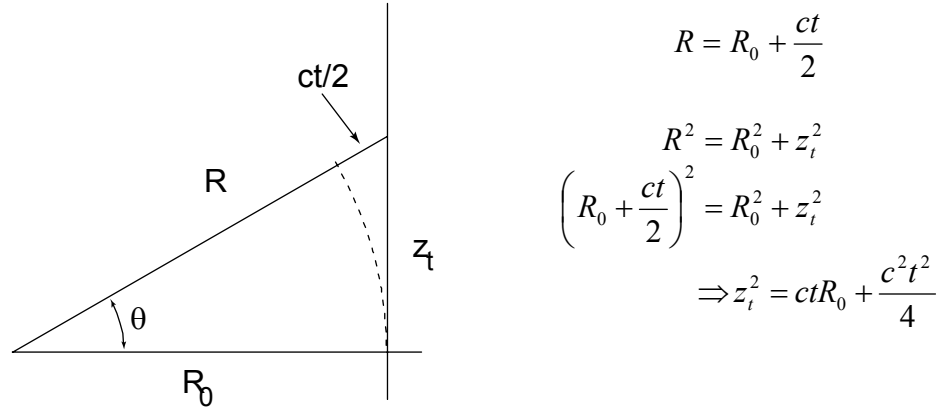
Note that we can factor out the $\cos^2 \theta$ term using $(\cos\theta)^{2a+b} = (\cos^2\theta)^{a+b/2}$. The following relations are derived from the above diagram, starting with $\cos\theta = R_0/R$:

$$\cos^2\theta = \frac{R_0^2}{R_0^2 + z_t^2} \qquad (32)$$
$$= \frac{1}{1 + z_t^2/R_0^2}$$

$$R^2 = z_t^2 + R_0^2 \qquad (33)$$

$$z_t = \sqrt{ctR_0\left(1 + \frac{ct}{4R_0}\right)} \qquad (34)$$

These are required because the integral we wish to solve does not have the variable z appearing explicitly in the integrand. Substitution into the following equation, carried over from the previous page,

$$P_R(t) = \frac{P_T \lambda^2 G^2(0) \sigma^0(0)}{32\pi^2} \int_0^{z_t} \frac{(\cos^2\theta)^{a+b/2}}{R^4} z\, dz \qquad (35)$$

results in

$$P_R(t) = \frac{P_T \lambda^2 G^2(0)\sigma^0(0)}{32\pi^2} \int_0^{z_t} \frac{\left(1/\left(1+z^2/R_0^2\right)\right)^{a+b/2}}{\left(z^2+R_0^2\right)^2} z\,dz$$

$$= \frac{P_T \lambda^2 G^2(0)\sigma^0(0)}{32\pi^2 R_0^4} \int_0^{z_t} \frac{z}{\left(1+z^2/R_0^2\right)^k}\,dz \qquad (36)$$

where $k = 2+a+b/2$. The variable z now appears explicitly in the integrand. Performing the integration, received power from the wall is

$$P_R(t) = \frac{P_T \lambda^2 G^2(0)\sigma^0(0)}{32\pi^2 R_0^2}\frac{1}{2(k-1)}\left\{1-\left(1+\frac{z_t^2}{R_0^2}\right)^{1-k}\right\}. \qquad (37)$$

Writing out the explicit time dependence of z_t, we have

$$1+\frac{z_t^2}{R_0^2} = \left(1+\frac{ct}{2R_0}\right)^2 \qquad (38)$$

$$P_R(t) = \frac{P_T \lambda^2 G^2(0)\sigma^0(0)}{32\pi^2 R_0^2}\frac{1}{2(k-1)}\left\{1-\frac{1}{\left(1+ct/2R_0\right)^{2(k-1)}}\right\} \qquad (39)$$

The time reference $t = 0$, is set when the leading edge of the transmit pulse is received after being reflected from the nearest part of the wall. The area of the wall is illuminated for $t < \tau$, at which point the center of the illuminated area opens up forming a ring of illumination.

The return signal can be separated into two regimes, where the first is increasing power as the direct return impinges on the receiver. The duration of this is equal to the pulse width, τ. After that, the signal power drops off, but at a reduced rate depending on the smoothness of the wall. The rougher the surface, the greater will be the range of scattering angles. This translates into a slower drop-off for the received power. Beyond time τ, the received power is due to an expanding ring on the wall surface. To obtain this contribution, consider the following

$$P_F(t) = P_R(t) - P_R(t-\tau) \qquad (40)$$

for $t \geq \tau$. At $t = \tau$, we have $P_F(\tau) = P_R(\tau) - P_R(0)$.

Recall that

$$P_R(t) = \int_0^{z_t} P_R\, 2\pi z\,dz \qquad (41)$$

Where we are integrating over the shaded area in the following diagram:
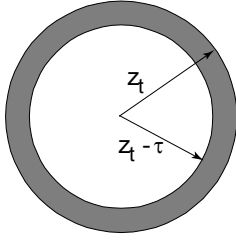
It follows that

$$P_F(t) = \int\limits_{z_{t-\tau}}^{z_t} P_R \, 2\pi z \, dz$$

$$= \int\limits_{z_{t-\tau}}^{0} P_R \, 2\pi z \, dz + \int\limits_{0}^{z_t} P_R \, 2\pi z \, dz \qquad (\,42\,)$$

$$= \int\limits_{0}^{z_t} P_R \, 2\pi z \, dz - \int\limits_{0}^{z_{t-\tau}} P_R \, 2\pi z \, dz$$

This last expression is rewritten as

$$P_F(t) = P_R(t) - P_R(t - \tau). \qquad (\,43\,)$$

An example of the pulse tail duration is given in Figure 42, where we have set $R_0 = 10$m, $\tau = 1$ ns, and the antenna beamwidth factor, $a = 2$.
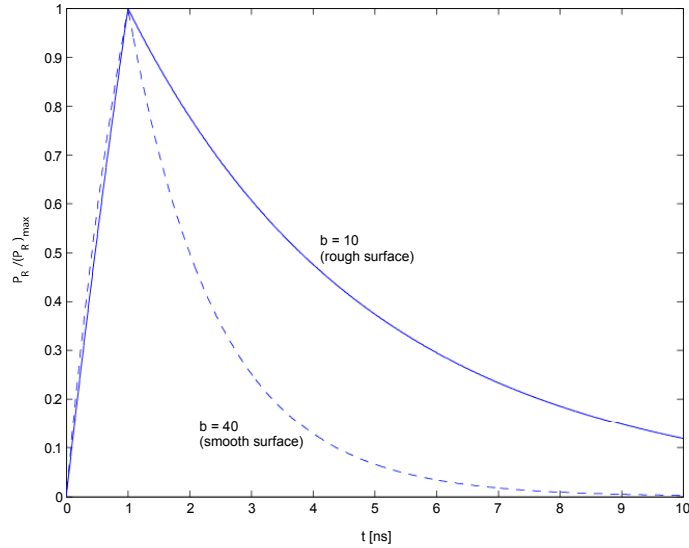
Figure 42. *Time signal of pulse returns.*

Having worked through the analytic details, it is relatively straight-forward to implement this in a few lines of code.

The plots in Figure 42 were produced using the Matlab routine in Table 6.

Table 6. Matlab code for wall clutter return pulse.

```
% -------------------- Wall Clutter ----------------------------
a = 2;          % antenna beamwidth factor
b = 10;          % surface roughness factor
          % (smooth surface; b large)
k = 2 + a + b/2;
gamma = 2*(k-1);
tau = 1.0;      % pulse width [ns]
c = 0.2998;     % [m/ns]
d = 10;          % range from wall [m]
tmax = 10;      % maximum delay [ns]
Xi = c/2/d;     % [1/ns]
A0 = 1;          % amplitude

del_t = 0.01;
t1 = 0:del_t:tau;
t2 = tau+del_t:del_t:tmax;

          % P_rise: power received as direct
          % pulse returns from wall extends
          % to t = tau, pulse duration
P_rise = A0*(1 - (1 + Xi*t1).^-gamma);
          % P_fall: power fall-off due to
          % finite range of incident angles
P_fall = A0*( (1 - (1 + Xi*t2).^-gamma)…
     - (1 - (1 + Xi*(t2-tau)).^-gamma) );

          % normalized plots
plot(t1,P_rise/max(P_rise))
hold on,plot(t2,P_fall/max(P_rise);
ylabel('P_R/(P_R)_{max}')
xlabel('t [ns]')
```

9.   Application to avalanche detection

One particular application of UWB impulse radar is to assist in search and rescue operations for avalanche victims. An obvious advantage of this technology is the ability to generate high-accuracy range data, while at the same time achieving good EM penetration with center frequencies less than two Gigahertz.

As mentioned in the introduction, portions of this work were sponsored by the Canadian National Search & Rescue Secretariat (NSS) to investigate the feasibility of using short-pulse UWB radar to detect objects buried in snow. This is a Canadian multi-department venture including Parks Canada, the NSS, and the Department of National Defence.

The experimental configuration [24] consisted of a large mound of snow, approximately 32 m^2, piled up next to a small building that housed the equipment. The snow-building boundary was composed of wood (plywood and 2 x 4's).

9.1   Range processing

In any two- or three-dimensional radar imaging system, the basic element of target information is a time-delayed impulse response. It is therefore convenient to first consider one-dimensional range data to assist with feasibility studies for such a system.

The objective of our experimental work was to measure radar returns from various objects buried in a mound of snow, examining the approximate SNR of the target response.

The results shown here are for a single transmitted pulse. No signal enhancement was obtained via pulse integration. Data processing consisted of application of a bandpass filter followed by background subtraction. Here, background subtraction reduced dynamic range ─ the initial impulse from the transmit antenna was removed, as well as reflections from a tunnel in the snow (used to place targets). This environment, in the absence of a target, formed the reference background.

Figure 43 shows returns from the snowbank, where various objects were placed. The wall, tunnel and snowbank acted as background reference, and was subtracted from each subsequent data set. The notation "AVH" denotes the type of pulse generator used in the experiment (Avtech Pulser model # AVH-HV1-C-T1). Range values need to be calibrated, but the targets appear at a relative range of ~2.3m, which is the approximate radial distance to targets.
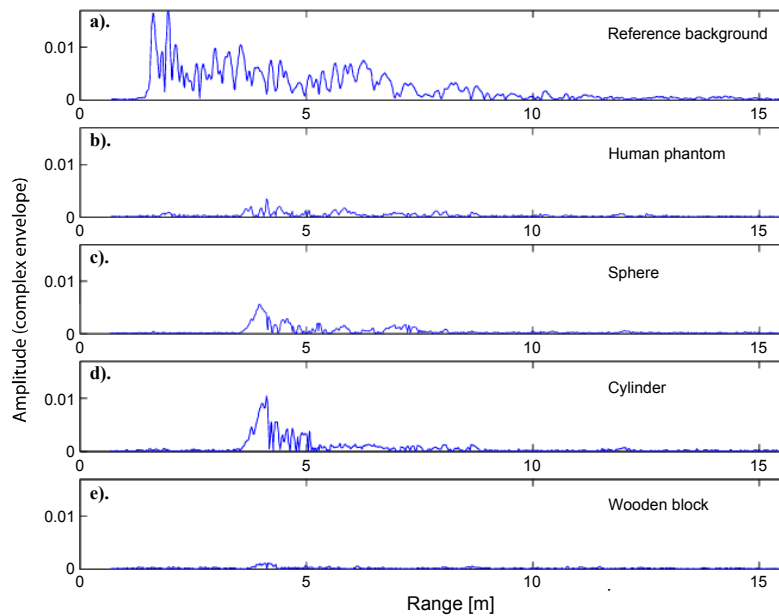
Figure 43. *Measured data after background subtraction for different buried targets.*

This data set consists of:

    a.   Reference return with snowbank and tunnel
         (All subsequent plots have this reference background subtracted).

    b.   Radar return from human phantom filled with saline

    c.   Radar return from a metallic sphere.

    d.   Radar return from metallic cylinder.

    e.   Radar return from a wooden block.

Target returns from the metallic objects display the largest values, while the wooden block produced the least reflections. Returns due to the human phantom lie between these two extremes and is clearly visible.

9.2 SAR processing

The system configuration (Figure 44) consists of one transmit antenna at coordinates (x=0.0, y=0.58, z=0.64)m. The receive antenna is moved along the x-axis, forming a synthetic array. In the experiment, there were five elements in the array at a spacing of 0.5m, generating an effective length of 2.0m. The y- and z- coordinates were fixed at zero. The imaging area has dimensions of 4m (azimuth) x 5m (range). The "wall" in this experiment is composed of plywood sheets acting as a boundary between the lab and the snowbank. The plywood is located 0.8m in front of the Rx array, and 0.2m in front of the Tx element.
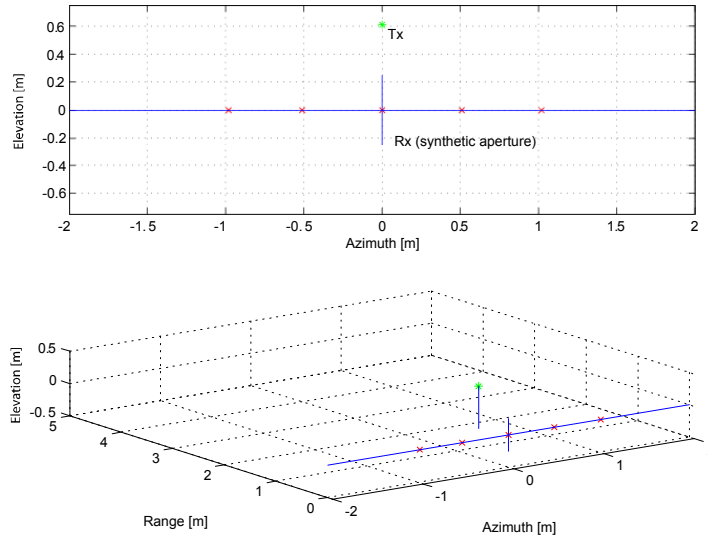
Figure 44. *Schematic showing the experimental configuration.*

9.2.1 Simulations

Sets of simulations corresponding to the experimental configuration were carried out, to determine if the qualitative features of SAR images could be reproduced. Within these simulations, two point reflectors were located at (x=-0.5, y=2.5, z=0.0)m; σ = 1.0 and (x=0.0, y=4.0, z=0.0)m; σ = 2.0. Here, the parameter σ denotes the reflection coefficient.

The first plot (Figure 45a) shows the image reconstruction using the five element positions as described previously, only now for a monostatic configuration. This means that Rx/Tx antennas are co-located and move along the synthetic aperture as one unit. Because of the greater angular diversity inherent in such a system, the resolving capability is better than that of the bistatic case (Figure 45b). For example, resolution can be characterized in terms of full-width at half-maximum (FWHM), and for the two cases, we obtain the following (In both cases, range = 2.5m, synthetic aperture length = 2m):

- Monostatic: FWHM = 1.1 m;
  Bistatic: FWHM = 1.7 m.

This yields a ratio of 0.65, close to the theoretical value of one-half obtained from comparison of a synthetic aperture vs. a physical array.

a).

b).
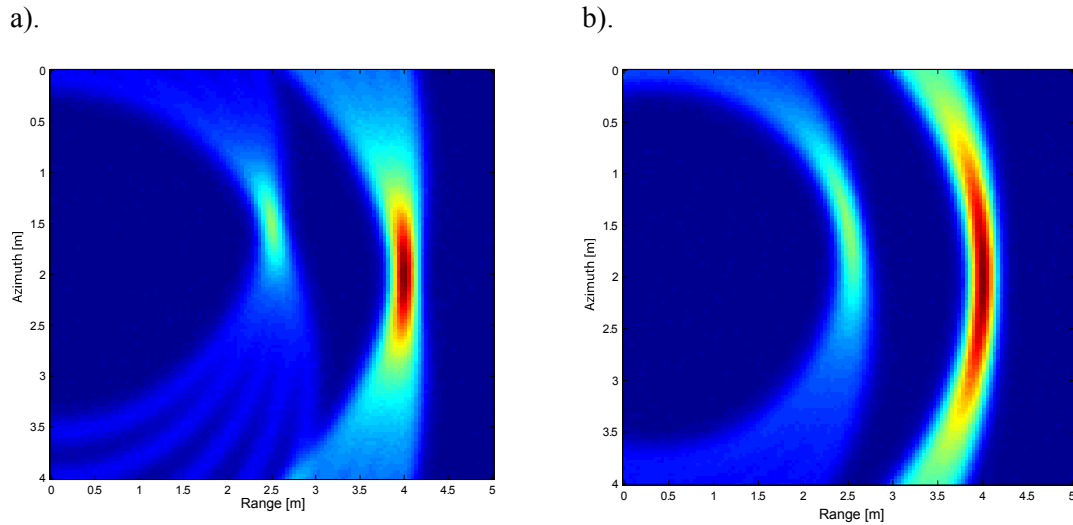
Figure 45. *Simulated data. a) Monostatic configuration, b) Bistatic configuration.*

Figure 46 shows a case where a "wall" has been simulated by generating a line of point reflectors. This is again for the bistatic case. The returns from desired targets are clearly present, but are severely reduced in relative magnitude compared with the wall returns. In the absence of the wall, this would revert back to the image depicted in Figure 45b. Somewhat artificially, the wall reflection coefficient has been set arbitrarily low at $\sigma = 0.5$, but even this shows how drastic the effect can be. This does not account for multipath, nor does it mimic propagation through a dielectric layer, but it does capture the effects of increased dynamic range.
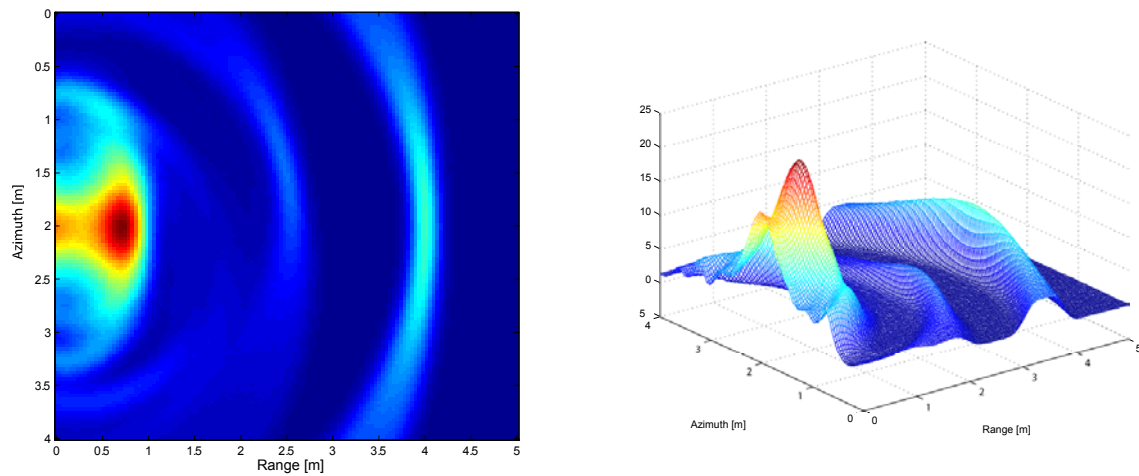
Figure 46. *Increased dynamic range accompanying the presence of a "wall" of point reflectors.*

9.2.2 Experimental data

The collected data was processed using the standard method of time-domain back projection to focus returns based on time delay. The kernel of this algorithm is the same as that used in simulations. Immediately we can see two of the same characteristics highlighted in simulated images: dynamic range and smearing out of target responses due to the bistatic configuration.

Figure 47 shows the processed data with wall returns. As expected, this dominates the image and the desired target (human phantom) is not at all obviously visible.
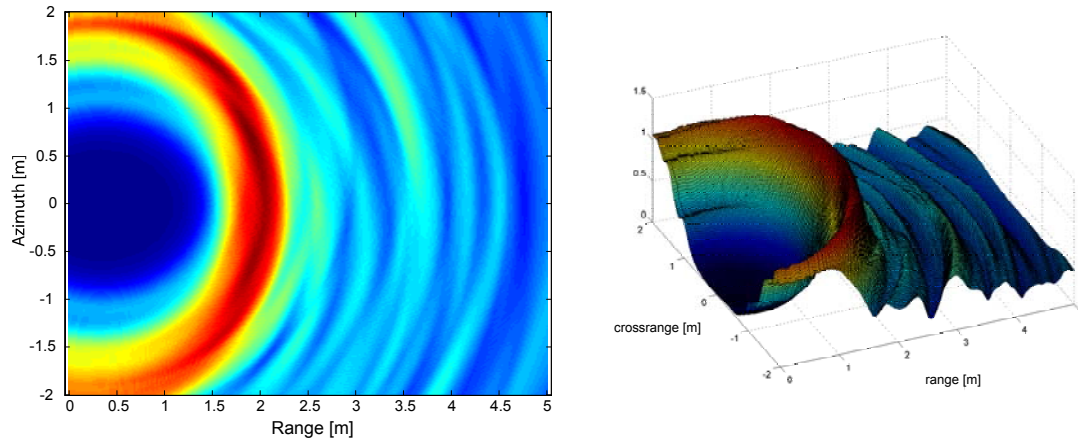
Figure 47. *No background subtraction. Wall returns dominate the image.*

To better view the target, the same scene without the human phantom was recorded and subsequently subtracted from the original image. The result is shown in Figure 48.
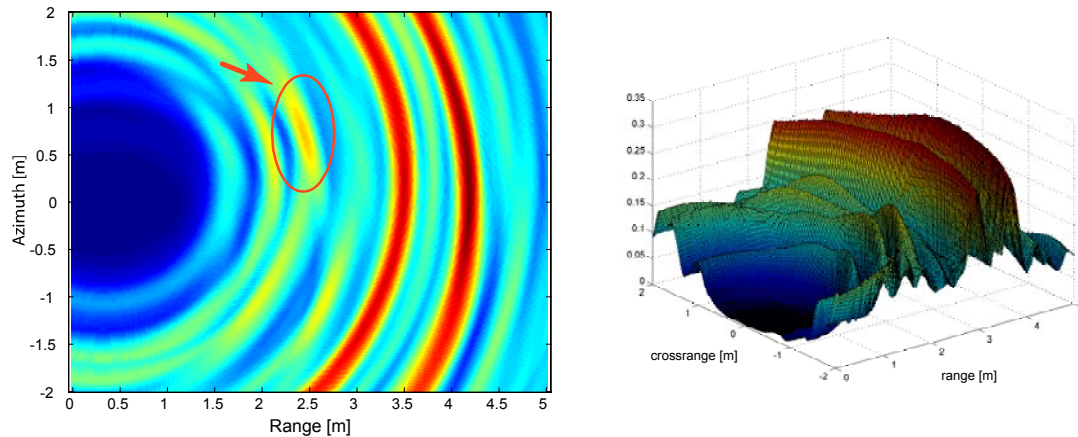
Figure 48. *With background subtraction. Wall returns negated, two strong reflectors beyond human phantom dominate the image.*

10. Discussion and Conclusions

UWB impulse radar is inherently a noise-limited technology. While sub-nanosecond pulses achieve good range resolution, the resultant extreme bandwidth extracts a toll on system performance in terms of noise power entering the receiver. As is typical of impulse radar returns that lack the filtering commonplace in narrowband systems, individual returns are severely impaired by thermal noise, clutter and external interference. Data must be processed efficiently to yield an acceptable signal to noise ratio (SNR), and to enhance structural details of the return pulse. This is achieved by a combination of ensemble averaging to reduce thermal fluctuations and the newly developed *Background Noise Conditioning* (BNC) method, a statistical signal processing technique used to remove isolated spectral interferers. BNC was developed at DRDC Ottawa to periodically examine spectral noise properties, and automatically configure an appropriate notch filter.

For the radar data presented, averaging over a relatively small number of pulses is insufficient to raise the desired returns appreciably above the noise floor. Typical SNR values at *N = 1* are around *18 to 19 dB*. Beyond ten pulses, SNR improves approximately linearly. Integration of about 80 pulses results in a SNR maximum of about *35 dB*, with an associated improvement of *~15 dB* over the untreated data (that is, for situations where BNC is not applied). For values *N > 80*, the averaging takes place over a long enough time period that returns become blurred due to target motion. This effectively defines the upper limit of *N* that can be achieved without additional processing to focus the returns.

Using the space-time backprojection technique, reconstructed data clearly shows the oscillatory motion of the target, but the signal vanishes as the radial velocity approaches zero at the two extremes of motion. Again using experimental data, we were able to verify the minimum detectable velocity for the system, depending on sampling increment, PRF and the number of pulses integrated, *N*. This information can be employed to construct a non-doppler MTI filter for target velocity discrimination. In turn, this could be used to further enhance SNR by time-aligning the integrated return pulses.

SNR is the metric that is most readily identifiable in characterizing radar detection. This, together with the radar range equation, becomes the basis for radar performance prediction. This model was employed semi-empirically, using parameter values that could either be measured directly or elucidated from available UWB experimental data, such as antenna gain, noise figure and background noise power. Independently, SNR and the path loss exponent were obtained directly from recorded data. Agreement with theoretical trends was quite good, although a recurrent issue is that close range data appears to have lower SNR than predicted. A tentative conclusion is that at close ranges, the system is unable to properly gate out the clutter returns, artificially raising the noise portion of the signal to noise ratio. This behaviour is also observed in the reconstructed ISAR images.

Part of this report is devoted to understanding and characterizing the impulse shape and its associated spectrum. Contrary to narrowband systems, bandwidth is determined less from pulse width than rise time. For example, a 0.5ns pulse width will not always translate to a 2GHz bandwidth, as is often reported in the literature. For the experimental system employed

here, the instrumentation produces a Gaussian pulse, where the pulse width and rise time are not independent parameters — specifying one fixes the other. Another issue related to proper characterization of a system is how the pulse width is defined. Due to its easy experimental access, we chose to use the full width at half maximum (FWHM) as the metric. From this, we had a center frequency of 380MHz, 3dB bandwidth of 220MHz, and an effective pulse width of 1.3 ns for an initial, transmit pulse width of 0.42ns.

A wall or similar dielectric boundary plays a role in the application of UWB systems. The two major concerns are attenuation and clutter. Taking a series of measurements, we were able to determine the cindercrete wall induced about 8 dB attenuation, while the same wall thouroughly wet caused only an additional 2dB loss (both of these are one-way measurements).

In through-wall imaging, the building material acts as a reflector, with its own characteristic RCS, σ. As the wall is an extended structure and not a point scatterer, it is convenient to express the RCS per unit area referred to as the normalized RCS, or backscatter coefficient. Using this as the starting point, we analyzed how the pulse would reflect off the wall, as a general function of the backscatter coefficient. An important consideration is that even though we consider normal incidence, there still exists a narrow range of angles over which the pulse interacts with the wall, leading to extended tails on the reflected pulses. This will lead to a better understanding of how to set the PRI to reduce this wall clutter.

Finally, we began to investigate imaging of objects buried in snow, using both 1D ranging and 2D SAR techniques. The results show that objects can be located, although the current resolution is such that it would make identification challenging. A major concern would be processing technique itself, where the ensemble averaging performs pulse-to-pulse subtraction to minimize thermal noise. This is a form of area MTI, where returns from stationary targets are partially removed in the processing stage. These results will be used to develop algorithms for extracting stationary targets without apriori knowledge of the background. One approach could be to establish a data bank of target signatures and use these to process data returns via correlation techniques.

11. References

1. Barrie, G. (2003). Ultra-wideband Synthetic Aperture Imaging – Data and Image Processing, (DRDC Ottawa TM 2003-015), Defence R&D Canada – Ottawa.

2. Gauthier, S., et. al. (2003). Surveillance Through Concrete Walls, (DRDC Ottawa TM 2003-233), Defence R&D Canada – Ottawa.

3. Gauthier, S., and Chamma, W. (2002). Through-The-Wall Surveillance. (DRDC Ottawa TM 2002-108), Defence R&D Canada – Ottawa.

4. Robinson, R. (2003). Through the Wall Ultra Wideband Radar. (DRDC-Ottawa CR 2003-023), Defence R&D Canada – Ottawa.

5. Barrie, G. & Tunaley, J. (2003). An Analysis of Through- and In-the-Wall UWB Impulse Radar: System Design Considerations, (DRDC Ottawa TM 2003-134), Defence R&D Canada – Ottawa.

6. Boutros, J. & Barrie, G. (2003). Ultra-wideband Synthetic Aperture Radar Imaging: Effect of off-track motion on resolution, (DRDC Ottawa TM 2003-177), Defence R&D Canada – Ottawa.

7. Barrie, G. (2003). Ultra Wideband Impulse Radar Data Exploitation, in Proc. of Euro Electromagnetics "EUROEM 2004," Magdeburg, Germany, pp.(UWB5-8, 145).

8. Hamming, R.W. (1989). Digital Filters, 3rd ed. Englewood Cliffs, NJ: Prentice-Hall.

9. Farr Research, Inc. (online) Ultra-Wideband Antenna Catalog, June 2004. http://www.farr-research.com (Nov. 2004).

10. Pelletier, M. and Luneau, P. (2003). Ultra-Wideband Radar Through-Wall Measurements. (DRDC Ottawa CR 2003-147). COMLAB Inc.

11. Luneau, P., et. al. (2004). 3D Through-Wall SAR Data and Imaging. (DRDC Ottawa CR 2004-103). COMLAB Inc.

12. Franceschetti, G., and Papas, C.H. (1974). Pulsed Antennas. IEEE Trans. Antennas Propagat., AP-22 (5), 651-661.

13. Jackson, J.D. (1998). Classical Electrodynamics 3rd ed. New York: Wiley.

14. Barton, D.K. (1976). Radar System Analysis. Dedham, MA: Artech. pp. 113.

15. TDS7000 Series digital Phosphor Oscilloscopes (TDS7407), Tektronix Inc., Beaverton, OR, US.

16. Sklar, B. (1988). Digital Communications, Englewood Cliffs, NJ: Prentice-Hall. pp. 202.

17. Chamma, W., and Kashyap, S. (2002). Detection of Targets Behind Walls Using Ultra Wide Band Short Pulse. In E. Mokole et.al., *Ultra-Wideband Short-Pulse Electromagnetics 6*, Plenum Press.

18. Gill, G.S., (1994). Waveform Generation and Signal Processing in Ultra Wideband Radar, SPIE Proc., Vol. 2235, 118-128.

19. L.M. Frazier. (1997). Radar Surveillance Through Solid Materials, SPIE, Vol. 2938, pp. 139-146.

20. L. Cai. (2000). Ultra-Wideband Model-Based Synthetic Aperture Radar Imaging Through Complex Media. Ph.D. Thesis, The Ohio State University.

21. Wangsness, R.K. (1986). Electromagnetic Fields, 2nd ed. Wiley, NY. pp. 405.

22. Schooley, A.H., (1956). Some Limiting Cases of Radar Sea Clutter Noise, Proc. IRE, Vol. 44, No. 8, pp. 1043-1047.

23. Levanon, N., (1988). Radar Principles. Wiley, NY. pp. 78.

24. Chamma, W., Mende, H., Barrie, G., and Robinson, R. (2004). Detection of Avalanche Victims using Ultra Wideband Short Pulse Radar. In E. Mokole et.al., *Ultra-Wideband Short-Pulse Electromagnetics 7*, Plenum Press. (In press).

List of acronyms

BNC   Background Noise Conditioning

DND   Department of National Defence

FWHM   Full Width at Half Maximum

ISAR   Inverse Synthetic Aperture Radar

LOS   Line of Sight

MTI   Moving Target Indicator

NSS   National Search and Rescue Secretariat

PRF   Pulse Repetition Frequency

PRI   Pulse Repetition Interval

RCS   Radar Cross Section

SAR   Synthetic Aperture Radar

DOCUMENT CONTROL DATA

(Security classification of title, body of abstract and indexing annotation must be entered when the overall document is classified)

1. ORIGINATOR (the name and address of the organization preparing the document. Organizations for whom the document was prepared, e.g. Establishment sponsoring a contractor's report, or tasking agency, are entered in section 8.)	2. SECURITY CLASSIFICATION (overall security classification of the document, including special warning terms if applicable)
Defence R&D Canada – Ottawa Ottawa, Ontario K1A 0Z4	UNCLASSIFIED

3. TITLE (the complete document title as indicated on the title page. Its classification should be indicated by the appropriate abbreviation (S,C or U) in parentheses after the title.)

    UWB Impulse Radar Characterization and Processing Techniques (U)

4. AUTHORS (Last name, first name, middle initial)

    Barrie, Greg, B.

5. DATE OF PUBLICATION (month and year of publication of document) December 2004	6a. NO. OF PAGES (total containing information. Include Annexes, Appendices, etc.) 76	6b. NO. OF REFS (total cited in document) 24

7. DESCRIPTIVE NOTES (the category of the document, e.g. technical report, technical note or memorandum. If appropriate, enter the type of report, e.g. interim, progress, summary, annual or final. Give the inclusive dates when a specific reporting period is covered.)

    Technical Report

8. SPONSORING ACTIVITY (the name of the department project office or laboratory sponsoring the research and development. Include the address.)

9a. PROJECT OR GRANT NO. (if appropriate, the applicable research and development project or grant number under which the document was written. Please specify whether project or grant) Project # 12KC15	9b. CONTRACT NO. (if appropriate, the applicable number under which the document was written)
10a. ORIGINATOR'S DOCUMENT NUMBER (the official document number by which the document is identified by the originating activity. This number must be unique to this document.) DRDC Ottawa TR 2004-251	10b. OTHER DOCUMENT NOS. (Any other numbers which may be assigned this document either by the originator or by the sponsor)

11. DOCUMENT AVAILABILITY (any limitations on further dissemination of the document, other than those imposed by security classification)

    (x) Unlimited distribution
    ( ) Distribution limited to defence departments and defence contractors; further distribution only as approved
    ( ) Distribution limited to defence departments and Canadian defence contractors; further distribution only as approved
    ( ) Distribution limited to government departments and agencies; further distribution only as approved
    ( ) Distribution limited to defence departments; further distribution only as approved
    ( ) Other (please specify):

12. DOCUMENT ANNOUNCEMENT (any limitation to the bibliographic announcement of this document. This will normally correspond to the Document Availability (11). However, where further distribution (beyond the audience specified in 11) is possible, a wider announcement audience may be selected.)

13. ABSTRACT (a brief and factual summary of the document. It may also appear elsewhere in the body of the document itself. It is highly desirable that the abstract of classified documents be unclassified. Each paragraph of the abstract shall begin with an indication of the security classification of the information in the paragraph (unless the document itself is unclassified) represented as (S), (C), or (U). It is not necessary to include here abstracts in both official languages unless the text is bilingual).

Ultra-Wideband (UWB) impulse radar is inherently a noise-limited technology. While sub-nanosecond pulses achieve good range resolution, the resultant extreme bandwidth exacts a toll on system performance in terms of noise power entering the receiver. Data must be processed efficiently to yield an acceptable signal to noise ratio (SNR), and to enhance structural details of the return pulse. This is achieved by a combination of ensemble averaging to reduce thermal fluctuations and the newly developed *Background Noise Conditioning* (BNC) method, a statistical signal processing technique used to remove isolated spectral interferers. BNC, developed at DRDC Ottawa, periodically examines spectral noise properties to automatically configure an appropriate notch filter.

For the radar data obtained in this investigation, averaging over a relatively small number of pulses is insufficient to raise the desired returns appreciably above the noise floor. Typical SNR values for one received pulse are around *18 to 19 dB*. Beyond ten pulses, SNR improves approximately linearly. Integration of about 80 pulses results in a SNR maximum of about *35 dB*, with an associated improvement of *~15 dB* over the untreated data (that is, for situations where BNC is not applied). For pulses *> 80*, the averaging takes place over a long enough time period that returns become blurred due to target motion. This effectively defines the upper limit of pulse returns that can be averaged without additional processing to focus the returns. Part of this report is devoted to modeling and characterizing the impulse shape and its associated spectrum. As well, the minimum detectable target velocity is extracted from data and compared with theory, showing good agreement.

Wall effects have been investigated—there was an experimental determination of approximately 8dB attenuation losses due to a cindercrete wall. The same wall, once soaked with water, caused only an additional 2dB loss (both of these are one-way measurements). A model for wall-induced clutter is developed, providing expressions for the pulse return shape and duration. The imaging of objects buried in snow, using both 1D ranging and 2D SAR techniques establishes that objects can be located, although the current resolution is such that it would make identification challenging. A major concern is the processing technique itself, which is a form of area Moving Target Indicator (MTI), where returns from stationary targets are partially removed in the processing stage. These results will be used to develop algorithms for extracting stationary targets without apriori knowledge of the background.

14. KEYWORDS, DESCRIPTORS or IDENTIFIERS (technically meaningful terms or short phrases that characterize a document and could be helpful in cataloguing the document. They should be selected so that no security classification is required. Identifiers such as equipment model designation, trade name, military project code name, geographic location may also be included. If possible keywords should be selected from a published thesaurus. e.g. Thesaurus of Engineering and Scientific Terms (TEST) and that thesaurus-identified. If it is not possible to select indexing terms which are Unclassified, the classification of each should be indicated as with the title.)

Ultra-Wideband radar, Impulse radar, through-wall imaging, through-wall sensing, wall attenuation, synthetic aperture radar.

Defence R&D Canada

Canada's leader in defence
and national security R&D

R & D pour la défense Canada

Chef de file au Canada en R & D
pour la défense et la sécurité nationale

DEFENCE R&D DÉFENSE